

Uncertainties with low-resolution nuclear forces

T. Plies ^{1, 2, *} M. Heinz ^{3, 4, 1, 2, 5, †} and A. Schwenk ^{1, 2, 5, ‡}

¹ Technische Universität Darmstadt, Department of Physics, 64289 Darmstadt, Germany

² ExtreMe Matter Institute EMMI, GSI Helmholtzzentrum für Schwerionenforschung GmbH, 64291 Darmstadt, Germany

³ National Center for Computational Sciences, Oak Ridge National Laboratory, Oak Ridge, TN 37831, USA

⁴ Physics Division, Oak Ridge National Laboratory, Oak Ridge, TN 37831, USA

⁵ Max-Planck-Institut für Kernphysik, Saupfercheckweg 1, 69117 Heidelberg, Germany

Low-resolution nuclear Hamiltonians, obtained from chiral effective field theory (EFT) and softened using renormalization group techniques, have been very successful in nuclear structure theory. The associated EFT truncation uncertainty for these potentials is difficult to quantify. We use singular values decompositions of low-resolution nuclear forces to obtain an operator basis to study Hamiltonian uncertainties for these potentials. We perform Bayesian inference for the singular values and three-body low-energy constants, the free parameters of nuclear Hamiltonians in our framework, using likelihoods based on nucleon-nucleon phase shifts and triton observables to account for the EFT truncation uncertainties in these quantities. We propagate the resulting distribution of Hamiltonians forward to predictions for ground-state properties of $^{24,28}\text{O}$ and ^{48}Ca , comparing against other state-of-the-art nuclear structure predictions. Our approach makes it possible to account for EFT uncertainties when using low-resolution potentials, which is important for many ongoing studies in exotic nuclei.

I. INTRODUCTION

Uncertainty quantification is a key aspect of modern nuclear theory. Theories of nuclear forces and most many-body methods are approximate, and the uncertainties associated with these approximations must be quantified. Chiral effective field theory (EFT) provides a systematically improvable description of nuclear forces rooted in quantum chromodynamics [1–3]. Such forces have several sources of uncertainty, due to the truncation of the EFT, how the forces are regularized, and how they are fit to data. Recent advances in Bayesian uncertainty quantification have enabled systematic approaches to quantifying theoretical uncertainties from various sources and propagating them to nuclear observables [4–12].

A notable gap in this body of work is uncertainty quantification for low-resolution Hamiltonians from chiral EFT [13], which have been successful in providing accurate predictions for nuclear structure. An interaction that stands out in the accurate description of binding energies and spectra across the nuclear chart is the 1.8/2.0 (EM) interaction [14–20]. Despite this remarkable accuracy, the uncertainties of this Hamiltonian are notoriously difficult to quantify. Recent works have significantly advanced the quality of uncertainty estimates for nuclear structure observables [10, 11]. We aim to do the same for low-resolution Hamiltonians, combining their historical success with modern uncertainty quantification methods.

A key barrier to performing Bayesian inference and robust uncertainty quantification for low-resolution Hamiltonians is the lack of an explicit operator basis. Low-resolution Hamiltonians are produced through nonlinear

renormalization group (RG) transformations. The RG transformations make them amenable to many-body calculations but destroy the underlying analytic structure of the potentials that is typically leveraged for uncertainty quantification. While EFT truncation uncertainty estimates for such potentials are possible in some prescriptions [21, 22], a complete treatment of uncertainties, going from few-body observables to Bayesian inference for low-energy constants (LECs) to posterior predictive distributions for nuclear structure [10], is still missing.

In this work, we overcome this barrier by leveraging data-driven singular value decompositions (SVDs) of nuclear forces. Such decompositions have been demonstrated to precisely reproduce the input Hamiltonians using only a few terms, meaning such decompositions effectively expose a low-rank operator basis for nuclear Hamiltonians [23–26]. Based on such decompositions, we are able to use state-of-the-art Bayesian uncertainty quantification approaches to account for EFT truncation uncertainties when using low-resolution Hamiltonians. We apply these developments to study the structure of neutron-rich oxygen and calcium isotopes.

This paper is structured as follows: In Sec. II, we describe the decomposition of low-resolution NN potentials and our selection of appropriate parameters. In Sec. III, we define our error models for NN phase shifts and triton observables. We construct likelihoods based on the truncation uncertainties of these observables, perform Bayesian inference, sample the resulting posterior, and analyze posterior predictive distributions to check the consistency of our model. In Sec. IV, we apply the resulting posterior distributions to ground-state properties of $^{24,28}\text{O}$ and ^{48}Ca to investigate how EFT truncation uncertainties in few-body systems propagate to observables in medium-mass nuclei. Finally, we conclude in Sec. V.

* tom.plies@tu-darmstadt.de

† heinzmc@ornl.gov

‡ schwenk@physik.tu-darmstadt.de

II. LINEAR OPERATOR STRUCTURE

Modern nuclear interactions derived from chiral EFT naturally exhibit a linear operator structure, where different contributions are summed up to compute the potential at a certain order [1, 2]. For example, the leading order (LO) potential is

$$V_{\text{LO}} = V_{\text{ct}}^{(0)} + V_{1\pi}^{(0)} = C_S + C_T \vec{\sigma}_1 \cdot \vec{\sigma}_2 + V_{1\pi}^{(0)}, \quad (1)$$

where $V_{1\pi}$ is the one-pion-exchange potential and $V_{\text{ct}}^{(0)}$ are the LO contact interactions. $\vec{\sigma}_1$ and $\vec{\sigma}_2$ denote the nucleon spin operators, and C_S and C_T are LECs. This allows us to write chiral EFT Hamiltonians as

$$H(\mathbf{c}) = H_0 + \sum_i c_i H_i, \quad (2)$$

where H_0 contains the parameter-free potential terms and the kinetic energy, and c_i and H_i are LECs and the associated operators in the parameter-dependent part of the Hamiltonian.

This linear structure facilitates a systematic statistical treatment of truncation uncertainties in chiral potentials. It allows for the construction of efficient eigenvector continuation (EC) emulators for the calculation of observables [27–29]. Eigenvector continuation emulators profit from a linear operator structure of the Hamiltonian by obtaining low-rank projections of the operators H_0 and H_i . The resulting EC matrix may then be quickly constructed and diagonalized as the LECs are varied. Using such emulators, one can perform Bayesian inference for the LECs, arriving at a joint distribution for all LECs corresponding to a distribution of Hamiltonians [10, 11, 30–36]. To propagate this Hamiltonian uncertainty to other nuclear structure observables, one then samples Hamiltonians from this distribution, where the linear structure again makes it easy to construct the Hamiltonian for each sample: one simply sums up the operators H_i together with the sampled c_i .

In practice, this linear operator structure is not always present for all chiral EFT interactions. One of the most widely used interactions is the 1.8/2.0 (EM) interaction [14], which has been successfully applied to a range of nuclear structure calculations [15–20]. The potential is constructed from the $N^3\text{LO}$ NN interaction by Entem and Machleidt (EM) with a 500 MeV cutoff [37], evolved to $\lambda = 1.8 \text{ fm}^{-1}$ through the similarity renormalization group (SRG) [38], and an unevolved $N^2\text{LO}$ 3N interaction with a cutoff of $\Lambda_{3\text{N}} = 2 \text{ fm}^{-1}$. The 3N LECs are fit to the ^3H ground-state energy and ^4He point-proton radius. The SRG evolution of the NN part improves convergence in many-body calculations [13, 39], but sacrifices the linear operator structure present in chiral EFT potentials [38]. For conventional generator choices, the SRG flow equation is quadratic in the potential, meaning that different terms mix in nontrivial ways through the SRG evolution. This leaves the evolved potential in a state where the original linear operator structure cannot be analytically recovered.

In this section, we aim to decompose SRG-evolved chiral potentials to recover a linear operator structure. In subsequent sections, we then leverage this decomposition for uncertainty quantification, the development and deployment of efficient emulators, and the easy evaluation of posterior predictive distributions for nuclear structure observables.

A. Decomposition of the potential

We use the singular value decomposition to construct a new operator basis. The resulting data-driven operators do not have a clear physics interpretation, but provide a quantitative reproduction of NN potentials using only a few leading terms [23].

The SVD decomposes any $m \times n$ matrix V into the product of three matrices

$$V = L S R^\dagger, \quad (3)$$

with the left and right matrices L and R^\dagger and the singular value matrix $S = \text{diag}(s_i)$, where s_i are the nonnegative singular values ordered with decreasing magnitude. In general, L and R^\dagger are $m \times m$ and $n \times n$ unitary matrices, respectively. They are made up of the left and right singular vectors, the outer product of which forms the individual SVD operators. S has dimensions $m \times n$ and consists of nonnegative real values on its diagonal. When decomposing square $n \times n$ matrices, like for our V_{NN} potentials, the dimensions of L , R^\dagger , and S are also $n \times n$.

Rewriting Eq. (3) yields

$$V = \sum_i s_i |L_i\rangle \langle R_i|, \quad (4)$$

which clearly has a linear operator structure with the coefficients s_i and the associated operators O_i constructed as outer products of left and right vectors $|L_i\rangle \langle R_i|$. It is this linear operator structure that we leverage in this work. We decompose NN potentials in a momentum-space partial-wave basis,

$$V(p, p') = \langle p | (lS) J T M_T | V_{\text{NN}} | p' | (l'S) J T M_T \rangle, \quad (5)$$

with the final and initial orbital angular momenta l and l' , the two-body spin S , the two-body total angular momentum J , the two-body isospin T with projection M_T , and the absolute values of the outgoing and incoming relative momenta p and p' . The matrix $V(p, p')$ is decomposed in each partial wave, automatically preserving relevant symmetries of the potential, e.g., rotational invariance.

In Fig. 1, we show the first five SVD operators and associated singular values for the $^1\text{S}_0$ and $^3\text{S}_1$ partial waves of the $N^3\text{LO}$ EM 500 $\lambda = 1.8 \text{ fm}^{-1}$ interaction. In both partial waves the first operator is purely attractive. In both cases, we also identify a purely repulsive operator with strength at high momenta, O_2 in $^1\text{S}_0$ and O_4 in $^3\text{S}_1$. For higher s_i the operators start showing oscillatory

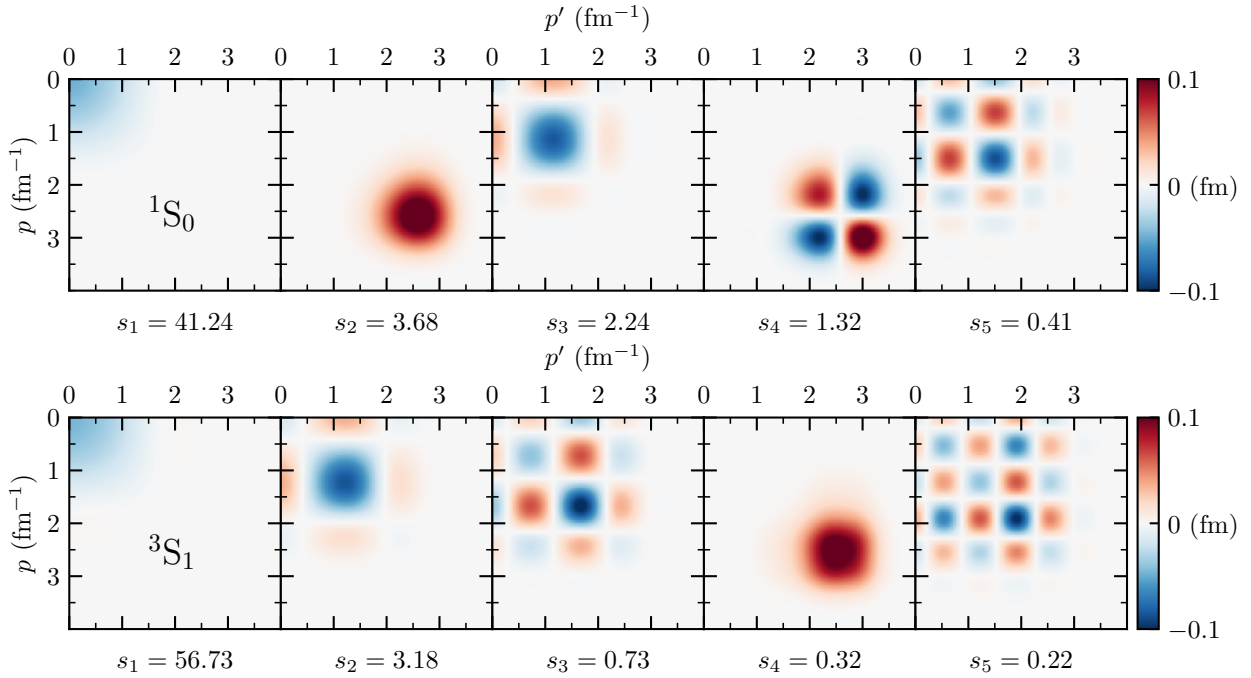


FIG. 1. First five SVD operators for the N^3LO EM 500 $\lambda = 1.8 \text{ fm}^{-1}$ potential in the 1S_0 (top panels) and 3S_1 (bottom panels) partial waves in momentum space representation $V(p, p')$. s_i are the singular values of the corresponding operators.

behavior. For both partial waves, s_5 is at least two orders of magnitude smaller than s_1 . This hierarchy of singular values allows us to use SVD-decomposed potentials truncated at rank five

$$\tilde{V} = \sum_{i=1}^{R_{\text{SVD}}=5} s_i |L_i\rangle \langle R_i|, \quad (6)$$

where R_{SVD} denotes the rank of the decomposition. It was shown in [23] that the first five out of the 100 operators of a decomposed potential are sufficient to reach accuracies above 99% for various observables. We are now left with SRG-evolved interactions in a linear operator structure for any partial wave, each depending on five parameters. We treat the parameters s_i as uncertain and seek to perform Bayesian inference for their values.

In order to better understand the impact of the operators, we individually vary the singular values of a partial-wave decomposed potential in an interval of $[0.5s_i, 1.5s_i]$. Afterwards, we compute the resulting phase shifts to understand which energies are affected by the individual operators. We also use this to identify operators that do not significantly affect phase shifts at the energies we are interested in. Those operators will not be varied in the future treatment of the potentials. This is done in order to reduce the number of parameters in our framework.

Figure 2 shows the resulting change in the phase shifts in the 3S_1 partial wave up to 200 MeV relative to the reference δ_{ref} , which is the result of solving the Lippmann-Schwinger equation with unvaried singular values. The gray band represents the EFT truncation uncertainty at N^3LO [following the EKM prescription as defined in

	1S_0	3S_1	1P_1	3P_0	3P_1	3P_2
s_1	x	x	x	x	x	x
s_2	—	x	x	—	—	x
s_3	x	x	x	—	x	x
s_4	—	—	—	x	x	—
s_5	x	—	—	—	—	—

TABLE I. Selection of singular values s_i for uncertainty propagation.

Eq. (10)]. Each panel shows the effects of varying a single singular value by various percentages. We easily identify that the fourth and fifth operators of this potential have negligible impact on phase shifts at energies below 200 MeV. We still keep these operators in the potential, but keep their respective singular values fixed.

Operators that barely affect phase shifts up to 200 MeV can be identified by their large high-momentum matrix elements. This can be seen in Fig. 1. The fourth and fifth operators have their largest matrix elements at momenta above 1.5 fm^{-1} , corresponding to a laboratory energy of 186 MeV. Looking at the three remaining operators, we observe that each of the operators appears to roughly affect phase shifts at different energies. This is important, as we aim to constrain the singular values through phase shifts at a range of energies up to 200 MeV. If all operators were to yield similar variations in phase shifts, we would not expect to be able to independently constrain our parameters and fully capture the EFT truncation uncertainties by calibrating to phase shift data.

In Table I, we identify three singular values to be var-

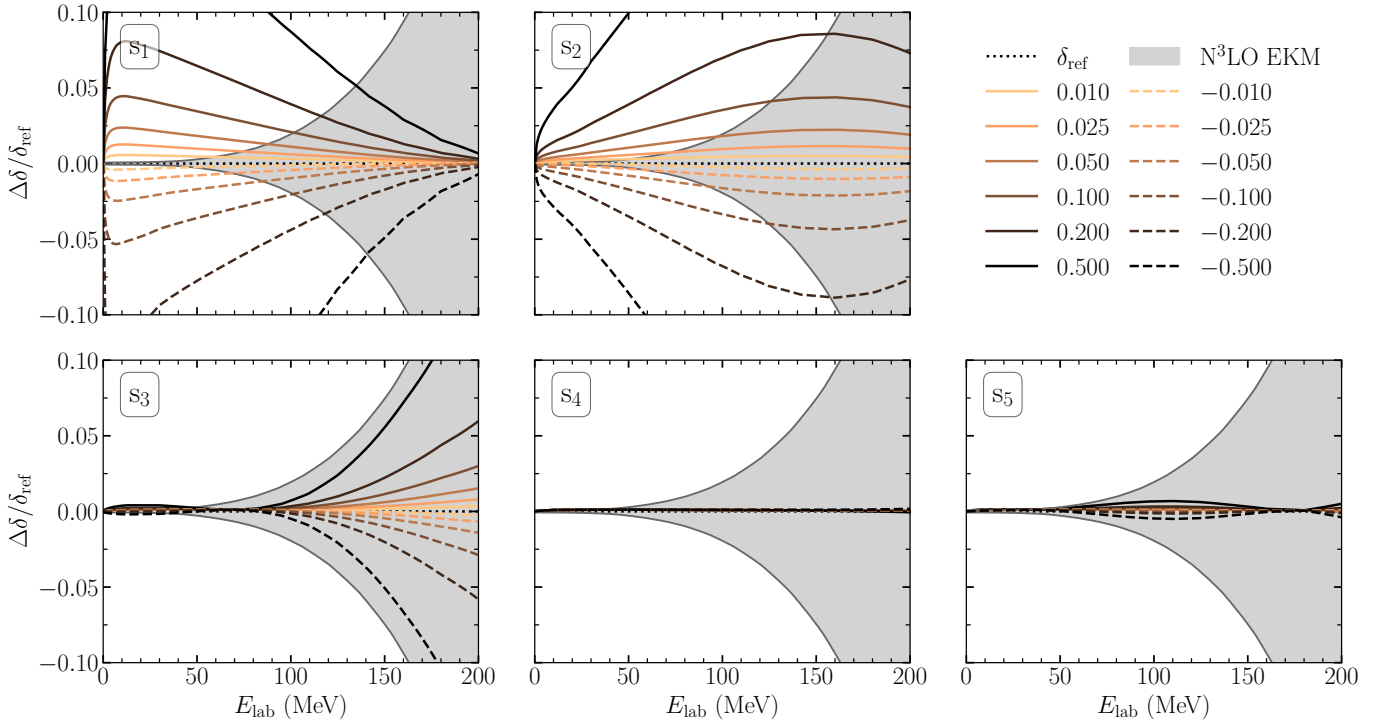


FIG. 2. Relative phase shifts for singular value variations in the 3S_1 partial wave. Each panel shows the change of phase shifts when varying one singular value at a time. Different colors represent varied singular values by a factor as given in the legend, where 0.5 stands for a singular value increased by 50%. Solid lines indicate positive factors while dashed lines stand for negative factors. The reference value is obtained by using the SVD-decomposed N^3LO EM 500 $\lambda = 1.8 \text{ fm}^{-1}$ interaction at rank five with the default set of singular values to solve the Lippmann-Schwinger equation. The gray band represents the relative EKM truncation uncertainty at N^3LO .

ied to capture phase shift uncertainties in each partial wave with the exception of 3P_0 , where we only find two appropriate singular values. This leaves us with 17 NN parameters in total. Note that we do not include higher order SVD operators beyond $R_{\text{SVD}} = 5$ for these partial waves, so subsequent results are subject to small SVD truncation errors, which we quantify. All other partial wave interactions are not SVD decomposed. With a parameter-dependent description of our potentials at hand, we can move on to performing statistical inference for these parameters.

III. EFT TRUNCATION UNCERTAINTIES

A successful approach to quantifying EFT uncertainties for observables assumes a power series expansion of the observable of interest y [5],

$$y = y_{\text{ref}} \sum_{n=0}^{\infty} c_n \left(\frac{Q}{\Lambda_b} \right)^n, \quad (7)$$

with the dimensionless coefficients c_n , the natural size of the observable y_{ref} , and the expansion parameter Q/Λ_b . This parameter consists of the momentum scale Q and the EFT breakdown scale Λ_b . For NN scattering, the relevant

momentum scale is set by $Q \equiv \max(p, m_\pi)$, where p is the relative momentum between two nucleons in the center-of-mass frame and m_π is the pion mass.

Truncating the EFT at finite order k also truncates this expansion,

$$y_k = y_{\text{ref}} \sum_{n=0}^k c_n \left(\frac{Q}{\Lambda_b} \right)^n. \quad (8)$$

The resulting error due to this truncation is simply the sum over all higher-order neglected terms:

$$\Delta y_k \equiv y_{\text{ref}} \sum_{n=k+1}^{\infty} c_n \left(\frac{Q}{\Lambda_b} \right)^n. \quad (9)$$

These higher-order corrections are generally unavailable to us, so we estimate the truncation uncertainty by the first omitted term $\Delta y_k \approx c_{k+1} (Q/\Lambda_b)^{k+1}$. To estimate the size of c_{k+1} , we follow the prescription of Epelbaum, Krebs, and Meißner (EKM) [6], assuming the coefficients c_n to be of natural size. The resulting uncertainty at

N^3LO is then given by

$$\Delta y_{\text{EKM}}^{N^3\text{LO}} = \max \left(\left(\frac{Q}{\Lambda_b} \right)^5 |y^{\text{LO}}|, \left(\frac{Q}{\Lambda_b} \right)^3 |y^{\text{LO}} - y^{\text{NLO}}|, \left(\frac{Q}{\Lambda_b} \right)^2 |y^{\text{NLO}} - y^{\text{N}^2\text{LO}}|, \left(\frac{Q}{\Lambda_b} \right) |y^{\text{N}^2\text{LO}} - y^{\text{N}^3\text{LO}}| \right). \quad (10)$$

When using the 1.8/2.0 (EM) interaction, applying this uncertainty quantification prescription to nuclear structure observables is challenging for several reasons. First, the 1.8/2.0 (EM) interaction is constructed from NN and 3N interactions at different orders. The NN interaction is at N^3LO in the chiral expansion, while the 3N interaction is at N^2LO . Second, this approach requires a definition of the momentum scale Q , which is difficult to define unambiguously for nuclei. It is however possible to infer the dimensionless expansion parameter Q/Λ_b using Bayesian methods [40–42].

To address these challenges, we use EFT uncertainties for observables in two- and three-body systems to construct a likelihood for our theory predictions. We perform Bayesian inference based on this likelihood to obtain a joint posterior distribution for the free parameters α_{NN} , c_D , and c_E in our NN and 3N potentials, where α_{NN} denotes all NN parameters and c_D and c_E are 3N LECs. Sampling from this distribution yields an ensemble of nuclear Hamiltonians that we can use in nuclear structure calculations. This allows us to propagate the EFT uncertainty captured in the posterior distribution to nuclear structure calculations.

A. NN uncertainties

We begin by constructing a likelihood function for the uncertainties in the NN interactions. In order to infer a distribution of the singular values, we incorporate data with Bayes' theorem. Specifically, for each partial wave, we infer distributions for s_i conditioned on phase shifts and their corresponding EFT truncation uncertainties.

Bayes' theorem allows us to capture truncation uncertainties of phase shifts while also implementing prior knowledge of the singular value distributions

$$\text{pr}(\alpha|\mathcal{D}) \propto \mathcal{L}(\alpha)\text{pr}(\alpha) = \text{pr}(\mathcal{D}|\alpha)\text{pr}(\alpha), \quad (11)$$

where $\text{pr}(\alpha|\mathcal{D})$ is the posterior probability of the set of singular values in a single partial wave given a set of data \mathcal{D} , which in our case are phase shifts [33]. $\mathcal{L}(\alpha) \equiv \text{pr}(\mathcal{D}|\alpha)$ is the likelihood. It expresses the conditional probability of \mathcal{D} given the parameters α . In our case, α are the three singular values that parametrize the NN potential in a single partial wave. $\text{pr}(\alpha)$ is the prior where we can implement prior knowledge or assumptions about the distribution of singular values. We use a uniform prior distribution on α with no lower and upper bounds.

Our goal is now to construct a likelihood function from NN phase shifts incorporating the EFT truncation uncertainties. By calculating the EKM uncertainties as defined in Eq. (10), with $\Lambda_b = 600$ MeV as suggested in [6], we obtain an interval around the reference phase shift at a given energy, $\Delta\delta_{\text{EKM}}(E)$. To assign probabilities at a given energy, we assume a Gaussian distribution for the EKM uncertainties with the standard deviation $\Delta\delta_{\text{EKM}}(E)$. The expectation value for this Gaussian is the reference phase shift obtained from using the default set of singular values.

Note that we need order-by-order results to assess uncertainties this way. However, the EM interaction is only available at N^3LO . We use the more recent EMN interactions [43], which are available up to N^4LO to calculate phase shifts at different chiral orders. We evolve these interactions to $\lambda = 2.0 \text{ fm}^{-1}$. The EMN interactions have the same cutoff of 500 MeV and the same regularization scheme, making them appropriate for estimating EFT uncertainties for the N^3LO EM interaction. The resulting truncation uncertainties for S- and P-wave phase shifts at different energies up to 300 MeV are given in Table II. For each partial wave and for each energy E , we end up with a Gaussian likelihood

$$f(\alpha, E) = \frac{1}{\Delta\delta_{\text{EKM}}(E)\sqrt{2\pi}} \exp \left(-\frac{(\delta_{\alpha}(E) - \delta_{\text{ref}}(E))^2}{2[\Delta\delta_{\text{EKM}}(E)]^2} \right), \quad (12)$$

based on the predicted phase shift $\delta_{\alpha}(E)$ and the reference phase shift $\delta_{\text{ref}}(E)$.

As phase shifts are given as a function of energy, we want to evaluate our likelihood at multiple energies as well. We construct a multivariate Gaussian for n different energies in the range between 0 MeV and 200 MeV. The upper bound of the interval is an assumption, realizing our focus on low energies. In Fig. 3, we visualize the construction of the NN likelihood for two different energy grids \mathbf{E}_1 and \mathbf{E}_2 defined in Sec. III C. The likelihood is then given by

$$\mathcal{L}(\alpha) = \frac{1}{\sqrt{(2\pi)^n \det(\Sigma)}} \times \exp \left(-\frac{1}{2} [\delta_{\alpha}(E) - \delta_{\text{ref}}(E)]^T \Sigma^{-1} [\delta_{\alpha}(E) - \delta_{\text{ref}}(E)] \right), \quad (13)$$

with the expectation value vector

$$\delta_{\text{ref}}(E) = (\delta_{\text{ref}}(E^{(1)}), \dots, \delta_{\text{ref}}(E^{(n)})), \quad (14)$$

and the singular-value-dependent phase shift result

$$\delta_{\alpha}(E) = (\delta_{\alpha}(E^{(1)}), \dots, \delta_{\alpha}(E^{(n)})). \quad (15)$$

Both are n -dimensional vectors. Their size is determined by the amount of energy points in our likelihood. The $n \times n$ covariance matrix is denoted as Σ . We assume in the definition of the covariance matrix Σ that there is zero

TABLE II. Absolute phase-shift uncertainties (in degree) at N³LO for S- and P-waves of the EMN 500 $\lambda = 2.0 \text{ fm}^{-1}$ interaction at different energies. Uncertainties are obtained through the EKM prescription.

E_{lab} (MeV)	$\Delta\delta_{1S_0}$	$\Delta\delta_{3S_1}$	$\Delta\delta_{1P_1}$	$\Delta\delta_{3P_0}$	$\Delta\delta_{3P_1}$	$\Delta\delta_{3P_2}$
1	$4.38 \cdot 10^{-2}$	$1.01 \cdot 10^{-1}$	$5.45 \cdot 10^{-4}$	$8.91 \cdot 10^{-4}$	$2.99 \cdot 10^{-4}$	$6.47 \cdot 10^{-4}$
5	$7.01 \cdot 10^{-2}$	$8.22 \cdot 10^{-2}$	$5.60 \cdot 10^{-3}$	$1.08 \cdot 10^{-2}$	$2.93 \cdot 10^{-3}$	$6.46 \cdot 10^{-3}$
10	$1.04 \cdot 10^{-1}$	$7.24 \cdot 10^{-2}$	$1.40 \cdot 10^{-2}$	$3.31 \cdot 10^{-2}$	$7.11 \cdot 10^{-3}$	$1.56 \cdot 10^{-2}$
20	$1.55 \cdot 10^{-1}$	$6.71 \cdot 10^{-2}$	$2.98 \cdot 10^{-2}$	$9.32 \cdot 10^{-2}$	$1.49 \cdot 10^{-2}$	$3.04 \cdot 10^{-2}$
30	$1.97 \cdot 10^{-1}$	$8.61 \cdot 10^{-2}$	$3.95 \cdot 10^{-2}$	$1.54 \cdot 10^{-1}$	$2.46 \cdot 10^{-2}$	$3.48 \cdot 10^{-2}$
50	$3.54 \cdot 10^{-1}$	$1.76 \cdot 10^{-1}$	$4.81 \cdot 10^{-2}$	$3.42 \cdot 10^{-1}$	$4.60 \cdot 10^{-2}$	$6.70 \cdot 10^{-2}$
75	$8.28 \cdot 10^{-1}$	$4.21 \cdot 10^{-1}$	$1.01 \cdot 10^{-1}$	$8.51 \cdot 10^{-1}$	$5.99 \cdot 10^{-2}$	$2.21 \cdot 10^{-1}$
100	$1.51 \cdot 10^0$	$8.35 \cdot 10^{-1}$	$2.30 \cdot 10^{-1}$	$1.53 \cdot 10^0$	$1.61 \cdot 10^{-1}$	$4.94 \cdot 10^{-1}$
150	$3.53 \cdot 10^0$	$2.25 \cdot 10^0$	$7.40 \cdot 10^{-1}$	$3.27 \cdot 10^0$	$7.66 \cdot 10^{-1}$	$1.39 \cdot 10^0$
200	$6.46 \cdot 10^0$	$4.42 \cdot 10^0$	$1.65 \cdot 10^0$	$5.43 \cdot 10^0$	$1.73 \cdot 10^0$	$2.58 \cdot 10^0$
300	$1.49 \cdot 10^1$	$1.14 \cdot 10^1$	$4.52 \cdot 10^0$	$1.05 \cdot 10^1$	$4.36 \cdot 10^0$	$4.91 \cdot 10^0$

correlation between the phase shifts at different energies

$$\Sigma = \begin{bmatrix} [\Delta\delta_{\text{EKM}}(E^{(1)})]^2 & & 0 \\ & \ddots & \\ 0 & & [\Delta\delta_{\text{EKM}}(E^{(n)})]^2 \end{bmatrix}. \quad (16)$$

In the future, we aim for a correlated treatment of phase shift uncertainties through the use of Gaussian processes [44].

We construct the combined likelihood for our NN potentials combining the individual likelihoods for the six partial waves

$$\mathcal{L}_{\text{NN}}(\boldsymbol{\alpha}_{\text{NN}}) = \mathcal{L}_{1S_0}(\boldsymbol{\alpha}_{1S_0})\mathcal{L}_{3S_1}(\boldsymbol{\alpha}_{3S_1})\mathcal{L}_{1P_1}(\boldsymbol{\alpha}_{1P_1}) \times \mathcal{L}_{3P_0}(\boldsymbol{\alpha}_{3P_0})\mathcal{L}_{3P_1}(\boldsymbol{\alpha}_{3P_1})\mathcal{L}_{3P_2}(\boldsymbol{\alpha}_{3P_2}), \quad (17)$$

by multiplying the individual likelihoods for each partial wave. The singular values from all S- and P-waves are collectively denoted $\boldsymbol{\alpha}_{\text{NN}}$. In doing so, we assume zero correlation between individual partial waves. The resulting likelihood \mathcal{L}_{NN} is a multivariate Gaussian with dimension $d = 6 \times \dim(\mathbf{E})$ for the chosen energy grid \mathbf{E} .

The main reason we only consider S- and P-waves is to limit the number of parameters in our model. The three parameters we assigned to each partial wave do not take into account different total isospin projections. Out of the six considered partial waves, only 3S_1 and 1P_1 appear in an isospin singlet. For partial waves 1S_0 , 3P_0 , 3P_1 , and 3P_2 , the isospin wave function must be symmetric, implying a total isospin quantum number $T = 1$ corresponding to a triplet state. This results in three distinct interactions within each partial wave, corresponding to the three projections of the total isospin. Since we determine three parameters to vary each potential, we would end up with $4 \times 3 \times 3 + 2 \times 3 \times 1 = 42$ parameters in total. We assume charge independence to reduce the number of parameters

$$V_{nn} \approx V_{np} \approx V_{pp} - V_C, \quad (18)$$

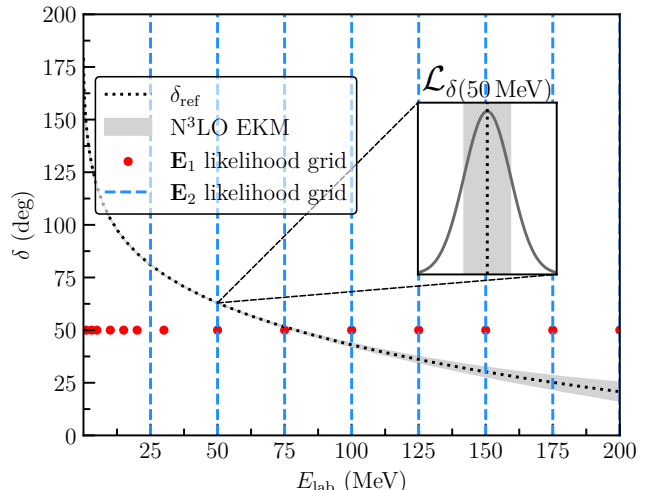


FIG. 3. Likelihood construction for phase shifts in a single partial wave. The dotted black line represents the reference phase shifts in the 3S_1 partial wave obtained by using the EM 500 $\lambda = 1.8 \text{ fm}^{-1}$ interaction at N³LO, SVD decomposed and truncated at rank five. The gray band indicates the EKM uncertainty at N³LO. Gaussian likelihoods are constructed at different energies according to the red points (\mathbf{E}_1) or the blue dashed lines (\mathbf{E}_2), defined in Eqs. (24) and (25).

with the Coulomb interaction V_C . This is realized by replacing both V_{nn} and $V_{pp} - V_C$ with V_{np} . After modifying the pp interaction through the charge independence assumption and the SVD, we add the unmodified Coulomb interaction to it. Now all interactions inside an isospin triplet depend on the same three parameters, reducing the number of parameters to $4 \times 3 \times 1 + 2 \times 3 \times 1 = 18$. We assess the validity of this approximation in Sec. IV. Note that we only use 17 NN parameters, as we limit ourselves to varying two parameters in the 3P_0 partial wave where only two of the largest five singular values

have a significant impact on phase shift variations over these energies.

B. 3N uncertainties

Three-nucleon forces first appear at $N^2\text{LO}$ in chiral EFT. These interactions are parametrized by five LECs c_1 , c_3 , c_4 , c_D , and c_E , where c_1 , c_3 , and c_4 also appear in the NN interactions. Similar to the two-nucleon interactions, we need to find a way to constrain these parameters. We limit ourselves to varying the two short-range LECs c_D and c_E and leave the long-range LECs c_i unchanged. Their values are fixed to $c_1 = -0.81$, $c_3 = -3.2$, and $c_4 = 5.4$ [37].

To infer distributions for the 3N LECs, we follow the work by Wesolowski *et al.* [41]. We choose the triton ground-state energy $E(^3\text{H})$ as well as the comparative triton half-life $fT_{1/2}$ [45] as additional observables for our full likelihood. These both depend on c_D and c_E , but also on all the NN singular values α_{NN} . We compute these observables using EC-based no-core shell model emulators [28] constructed by Takayuki Miyagi [46].

In order to construct a likelihood from these observables, we again start with Eq. (7), as we are interested in the EFT truncation error. However, this time we will not use the EKM uncertainties. Assuming the series coefficients c_n to be of natural size, we can use a constant \bar{c} , move it out of the power series, and write down the geometric series expression

$$(\Sigma)_{ij} = \left[\frac{(y_{\text{EM}} \bar{c} (\frac{Q}{\Lambda_b})^{k+1})^2}{1 - (\frac{Q}{\Lambda_b})^2} \right] \delta_{ij}, \quad (19)$$

where we use the 1.8/2.0 (EM) prediction y_{EM} as the characteristic size of the observable y [5, 9]. This gives us a diagonal covariance matrix as we do not assume any correlation between the observables. Since we use a single covariance matrix for multiple observables, the variables $\tilde{Q} \equiv Q/\Lambda_b$ and \bar{c} are determined globally for both of our observables. This was done in [41] by investigating the NLO to $N^2\text{LO}$ corrections of selected triton and helium observables and treating \tilde{Q} and \bar{c} as random variables. This results in a distribution for the two variables, we use their central values of approximately $\tilde{Q} = 1/3$ and $\bar{c} = 1$.

Using this covariance matrix, we construct a multivariate Gaussian as our 3N likelihood

$$\mathcal{L}_{3\text{N}}(c_D, c_E, \alpha_{\text{NN}}) = \mathcal{N}(\mathbf{y}_{\text{ref}}, \Sigma), \quad (20)$$

with the reference theoretical predictions from our emulators $\mathbf{y}_{\text{ref}} = (E(^3\text{H})_{\text{ref}}, fT_{1/2,\text{ref}})$ for a set of default parameters. For the NN interaction, we choose the unvaried singular values. For the 3N interaction, we use the fixed c_i values and $c_D = 1.264$ and $c_E = -0.12$ to calculate y_{ref} . Note that the likelihood also depends on the NN parameters α_{NN} .

With Bayes' theorem we arrive at an expression for the

TABLE III. Values denoted as y_{ref} are the results calculated with the emulator when using the default set of parameters. Deviations from the results obtained using the 1.8/2.0 (EM) interaction without an emulator, denoted as y_{EM} , mainly stem from the charge-independence assumption and the SVD truncation. The standard deviation σ is obtained using Eq. (19). Experimental results are shown in the last column for comparison.

	y_{ref}	y_{EM}	σ	Experiment
$E(^3\text{H})$ (MeV)	-8.69	-8.48	0.11	-8.48 [48]
$fT_{1/2}$ (s)	1228.76	1227.72 [46]	16.09	1129.6 [49]

distribution of the LECs

$$\text{pr}(c_D, c_E, \alpha_{\text{NN}} | E(^3\text{H}), fT_{1/2}) \propto \text{pr}(E(^3\text{H}), fT_{1/2} | c_D, c_E, \alpha_{\text{NN}}) \text{pr}(c_D, c_E, \alpha_{\text{NN}}), \quad (21)$$

with the prior $\text{pr}(c_D, c_E, \alpha_{\text{NN}})$ consisting of uniform distributions for c_D, c_E around their central values, and the uniform priors for the singular values. The parameter c_D has a prior range of $[-8.7, 11.3]$ and c_E has a range of $[-2.1, 1.9]$. These intervals have shown no noticeable effects on the posterior distribution. The likelihood $\mathcal{L}(c_D, c_E, \alpha_{\text{NN}}) \equiv \text{pr}(E(^3\text{H}), fT_{1/2} | c_D, c_E, \alpha_{\text{NN}})$ is conditioned on the truncation uncertainty of the triton binding energy and comparative half-life.

The comparative half-life of the triton is an electroweak observable, related to transition matrix elements by

$$fT_{1/2} = \frac{K/G_V^2}{\langle \hat{F} \rangle^2 + \frac{f_A}{f_V} g_A^2 \langle \hat{G}T \rangle^2}, \quad (22)$$

with $K/G_V^2 = 6147$, $f_A/f_V \approx 1$, and the axial-vector coupling constant $g_A = 1.27$ [47]. $\langle \hat{F} \rangle$ and $\langle \hat{G}T \rangle$ denote the reduced Fermi and Gamow-Teller matrix elements. We compute these using emulated ground-state wave functions. The Gamow-Teller transition involves the axial-vector current and is sensitive to two-body currents, which depend on the three-body LEC c_D , so it provides an effective tool to constrain 3N interactions [45].

Following Eq. (19), we obtain the standard deviations shown in Table III. We denote the results using the 1.8/2.0 (EM) interaction as y_{EM} and those using our emulators with default parameter values as y_{ref} in Table III. We notice that the emulator predictions deviate from the 1.8/2.0 (EM) results for the triton energy. The emulator uncertainty is below 1% [46]. The deviations between the emulator and the 1.8/2.0 (EM) predictions are primarily caused by the charge-independence assumption and the SVD truncation.

C. Sampling the posterior

To combine the likelihoods of the NN and the 3N interaction, we multiply

$$\mathcal{L}(c_D, c_E, \boldsymbol{\alpha}_{\text{NN}}) = \mathcal{L}_{\text{NN}}(\boldsymbol{\alpha}_{\text{NN}}) \mathcal{L}_{\text{3N}}(c_D, c_E, \boldsymbol{\alpha}_{\text{NN}}). \quad (23)$$

We cannot provide an analytical expression for this likelihood. Instead, we have to sample the posterior distribution. For this, we use the affine Markov chain Monte Carlo (MCMC) sampler `emcee` [50].

We use 100 walkers in total that are initialized around the default parameters. Each walker performs 10,000 steps to ensure stationarity, and the first 5,000 are discarded as burn-in. In total, we then have 500,000 samples from our MCMC sampling. To reduce this to a manageable amount of samples for nuclear structure studies, we subsample by randomly selecting a single sample from each walker, leaving us with a total of $N = 100$ samples. This can be seen as an extreme way of thinning the walkers, another way to reduce autocorrelation.

We find that the full NN posterior depends on the positions of the energies where we evaluate the individual likelihoods. To investigate the impact of the choice of these positions, we perform two independent runs with different energy grids for Eq. (16). The first one will use the energies

$$\mathbf{E}_1 = (1, 3, 5, 10, 15, 20, 30, 50, 75, 100, 125, 150, 175, 200) \text{ MeV}, \quad (24)$$

emphasizing low-energy phase shifts. This amounts to a total of 14 energies at which we evaluate the phase shifts. In the second run we will use only eight evenly spaced energies

$$\mathbf{E}_2 = (25, 50, 75, 100, 125, 150, 175, 200) \text{ MeV}. \quad (25)$$

Using \mathbf{E}_2 should reduce the error due to missing correlations, as we evaluate energies not too close to each other.

Phase-shift uncertainties are orders of magnitude smaller at low energies (~ 1 MeV) compared to larger energies (> 50 MeV), as seen in Table II. Evaluating the likelihood at such small energies puts strong constraints on the overall possible phase shifts and thereby on the underlying LEC combinations. We use the second run to investigate the impact of including low energies in the likelihood and also to investigate the influence of broader phase-shift and parameter distributions on the posterior predictive distributions.

We are left with $N = 100$ samples of our two- and three-body parameters $\{\tilde{\boldsymbol{\alpha}}_i\}_{i=1}^N$, where $\tilde{\boldsymbol{\alpha}} = \boldsymbol{\alpha}_{\text{NN}}, c_D, c_E$, according to the posterior distribution $\text{pr}(\tilde{\boldsymbol{\alpha}}|\mathcal{D})$. The full posterior distribution is shown in Fig. 4. These samples account for the truncation uncertainty of phase shifts in the S- and P-waves as well as those of the triton binding energy and the comparative half-life.

D. Posterior predictive distributions

In this section, we evaluate our sampling results through posterior predictive distributions (PPDs) of the same observables used for the Bayesian inference of the parameters $\tilde{\boldsymbol{\alpha}}$. This process is part of model checking. If the likelihood correctly encodes the data and model uncertainties and the priors are uninformative, the posterior distributions should reflect those uncertainties. We consider both runs using the energy grids \mathbf{E}_1 and \mathbf{E}_2 and separately analyze the NN and 3N components of our framework.

Using the sampled values for the parameters $\{\tilde{\boldsymbol{\alpha}}_i\}_{i=1}^N$, we compute the PPDs

$$\text{PPD} = \{\mathbf{y}(\tilde{\boldsymbol{\alpha}}) : \tilde{\boldsymbol{\alpha}} \sim \text{pr}(\tilde{\boldsymbol{\alpha}}|\mathcal{D})\}, \quad (26)$$

to assess the consistency of our parameter distributions. The posterior $\text{pr}(\tilde{\boldsymbol{\alpha}}|\mathcal{D})$ is the result of the MCMC sampling. When calculating phase shifts in a given partial wave, we effectively marginalize over c_D , c_E , and all $\boldsymbol{\alpha}_{\text{NN}}$ that correspond to different partial waves. The triton observables, on the other hand, depend on both NN and 3N parameters.

In Fig. 5, we compare PPDs for phase shifts in the 3S_1 partial wave before and after subsampling for the distributions obtained using the \mathbf{E}_2 likelihood. The individual plots show phase shift distributions at different energies. At each energy we observe the distributions as well as their associated 68% confidence intervals (CIs) to be very similar. We observe similar behavior in the other S- and P-waves. This validates our approximation to use only a fraction of the initial samples.

In Fig. 6, we compare phase shift distributions obtained using the \mathbf{E}_1 and \mathbf{E}_2 likelihood, again in the 3S_1 partial wave. Our main interest is to see how the posterior distributions compare to the distributions we assumed in the likelihood. Ideally, the distributions are identical, which we would observe as the EKM uncertainty (black dashed lines) and the 68% confidence intervals of the PPDs (red and blue dashed lines) aligning.

In practice, we observe deviations from these ideal expectations. Phase shift distributions over- and under-predict the EKM uncertainties, depending on the energy. Additionally, the choice of the likelihood, e.g., the energies at which we evaluate phase shifts in the NN likelihood impacts the posterior distributions of phase shifts. Considering again Fig. 2, we see that each operator affects phase shifts over a range of energies. We cannot expect to vary phase shifts independently over a range of 200 MeV with only three parameters that are not independent in the energies they impact. We will see later the reproduction of uncertainties further deteriorates when we only have two instead of three parameters, as is the case for phase shifts in the 3P_0 partial wave. We note, however, that simply extending the decomposition to higher ranks and allowing more singular values to vary within a single partial wave does not improve the reproduction of the input uncertainties. We simply lack the necessary independent degrees of freedom to fully reproduce the EFT

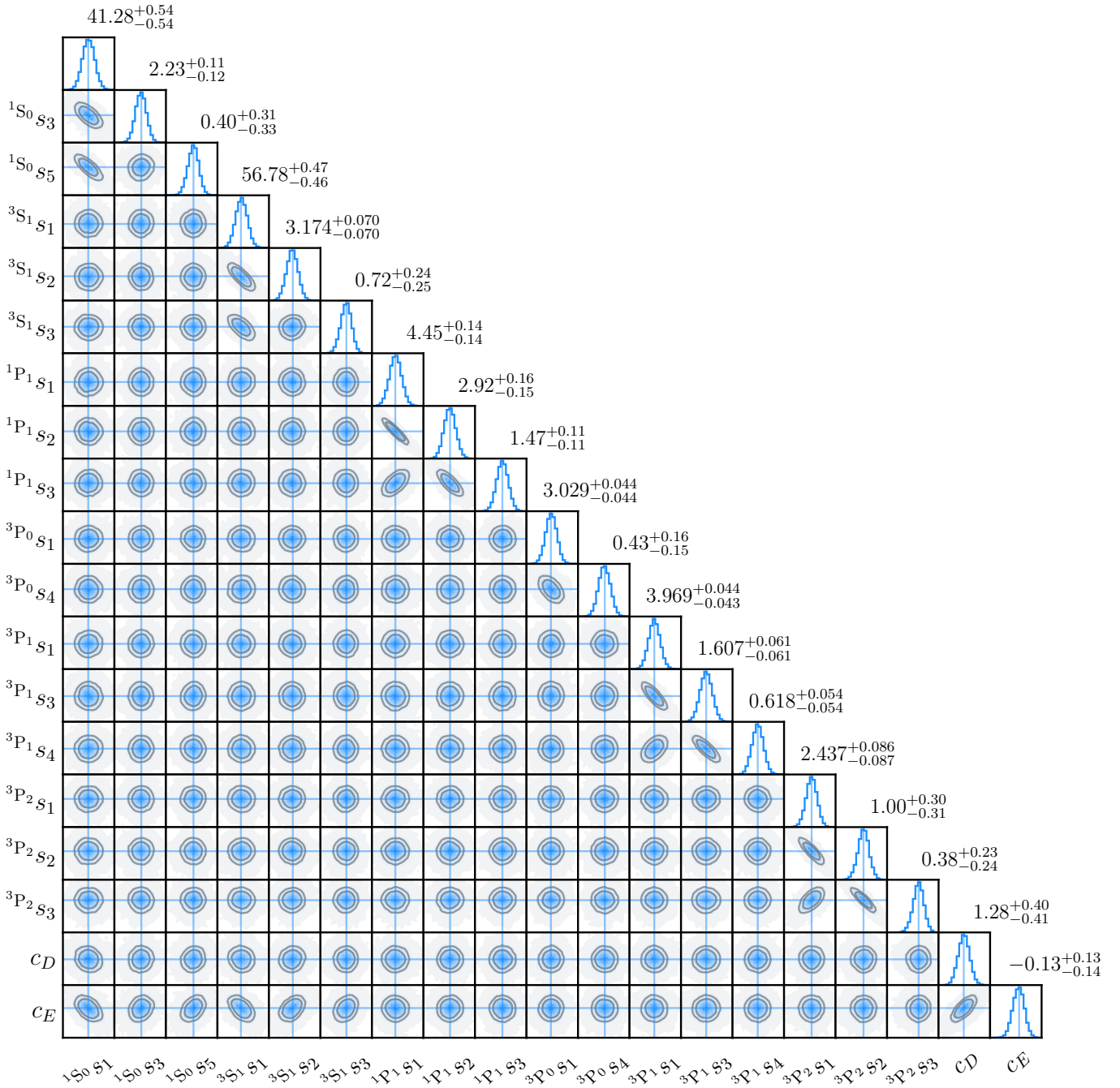


FIG. 4. Posterior distributions for the jointly sampled 17 NN and 2 3N parameters for all 5×10^5 samples. Distributions were obtained using the \mathbf{E}_2 likelihoods. Contours enclose 39% and 87% of the total probability, matching the fractions of a 1 σ and 2 σ contour for a 2D Gaussian. Values on top denote the median and the marginalized 68% confidence intervals.

uncertainties at all energies, which is unsurprising given that these are naturally also correlated and thus not fully independent as we conservatively assume.

Coming back to Fig. 6, we observe that at energies below 25 MeV, the \mathbf{E}_2 results overpredict the EKM uncertainty, reflecting the fact that we put no direct constraints on phase shifts at these energies. Only correlations with phase shifts at higher energies, which are directly included

in the likelihood, constrain these low-energy phase shifts. In contrast, the \mathbf{E}_1 likelihood already actively constrains phase shifts at 1 MeV, which yields narrower phase shifts distributions. The distributions using \mathbf{E}_1 are narrower than the initial EKM uncertainties. Going to higher energies, both distributions underpredict the EKM uncertainties, with significantly smaller 68% CIs starting at 100 MeV. The \mathbf{E}_2 distributions are broader than the \mathbf{E}_1

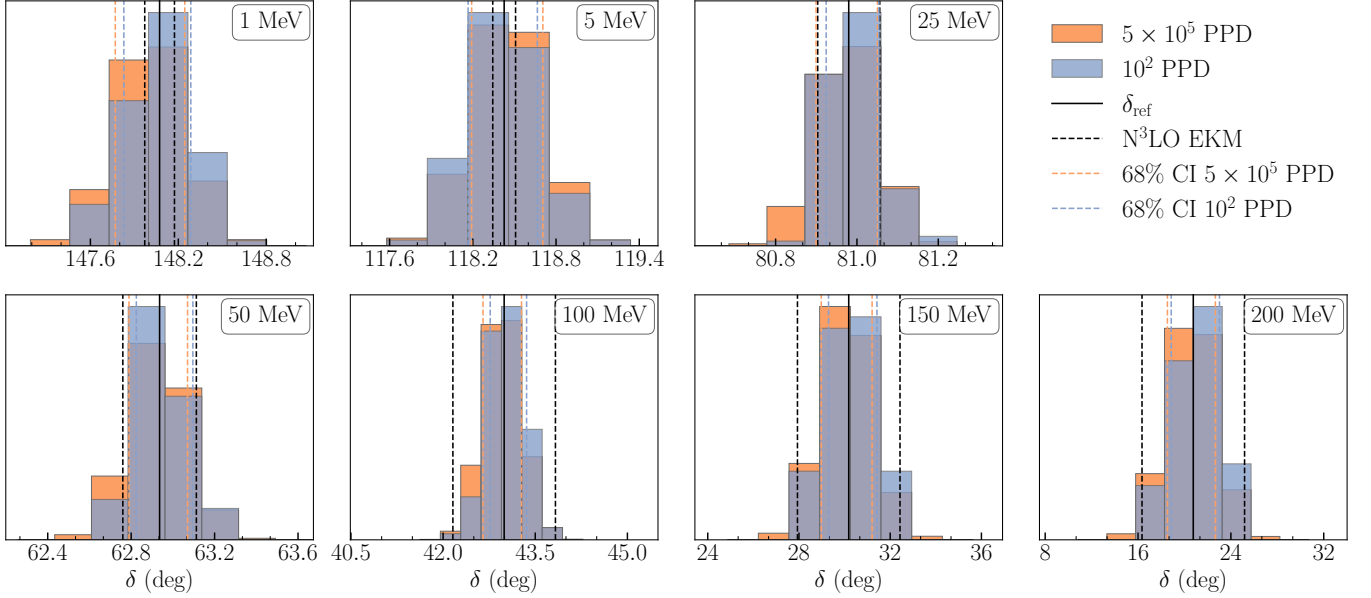


FIG. 5. Comparison of phase shifts PPDs in the 3S_1 partial wave for all 5×10^5 samples (red) and for the resampled 10^2 samples (blue) at different energies. Results were obtained using the E_2 likelihood. The red and blue dashed lines show the corresponding 68% confidence intervals. The solid black line represents the reference phase shifts obtained by using the SVD-decomposed N^3LO EM 500 $\lambda = 1.8 \text{ fm}^{-1}$ interaction at rank five. The black dashed lines represent the EKM uncertainty at N^3LO .

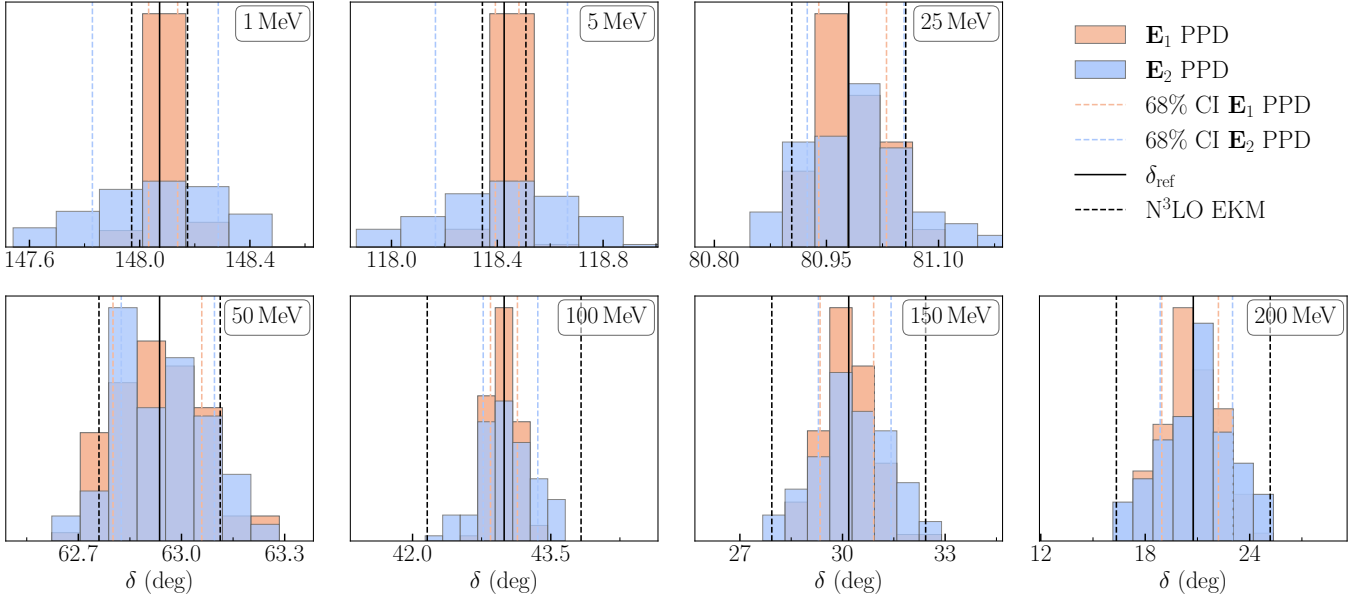
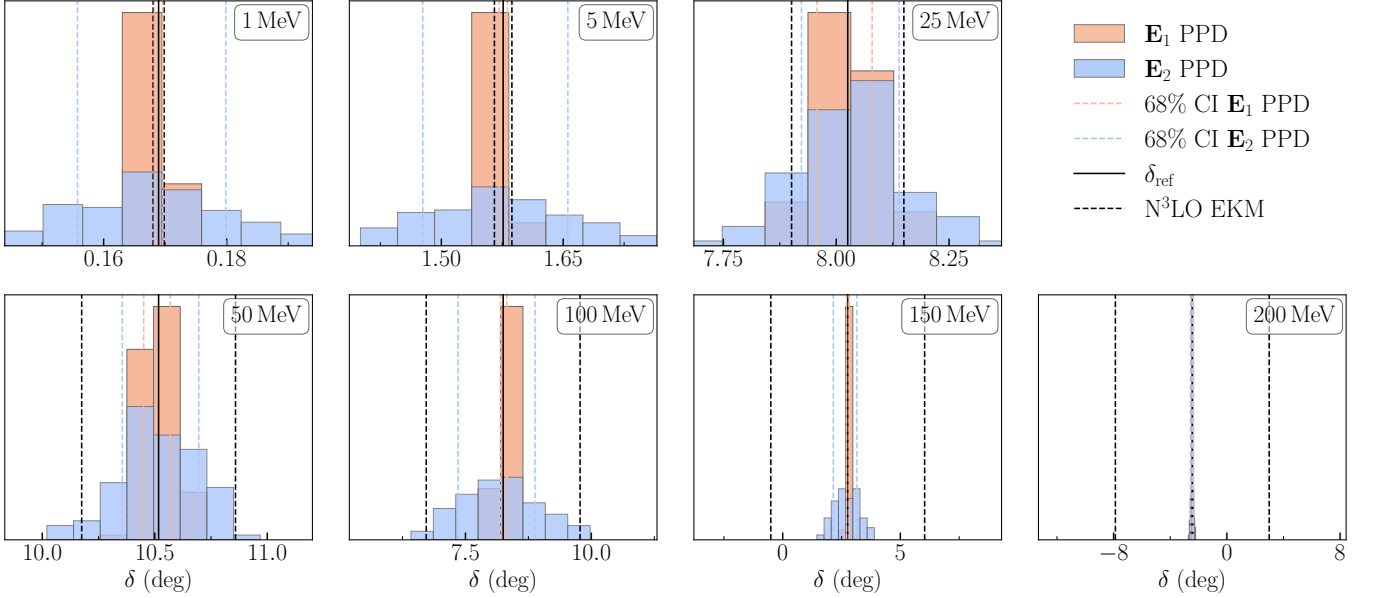
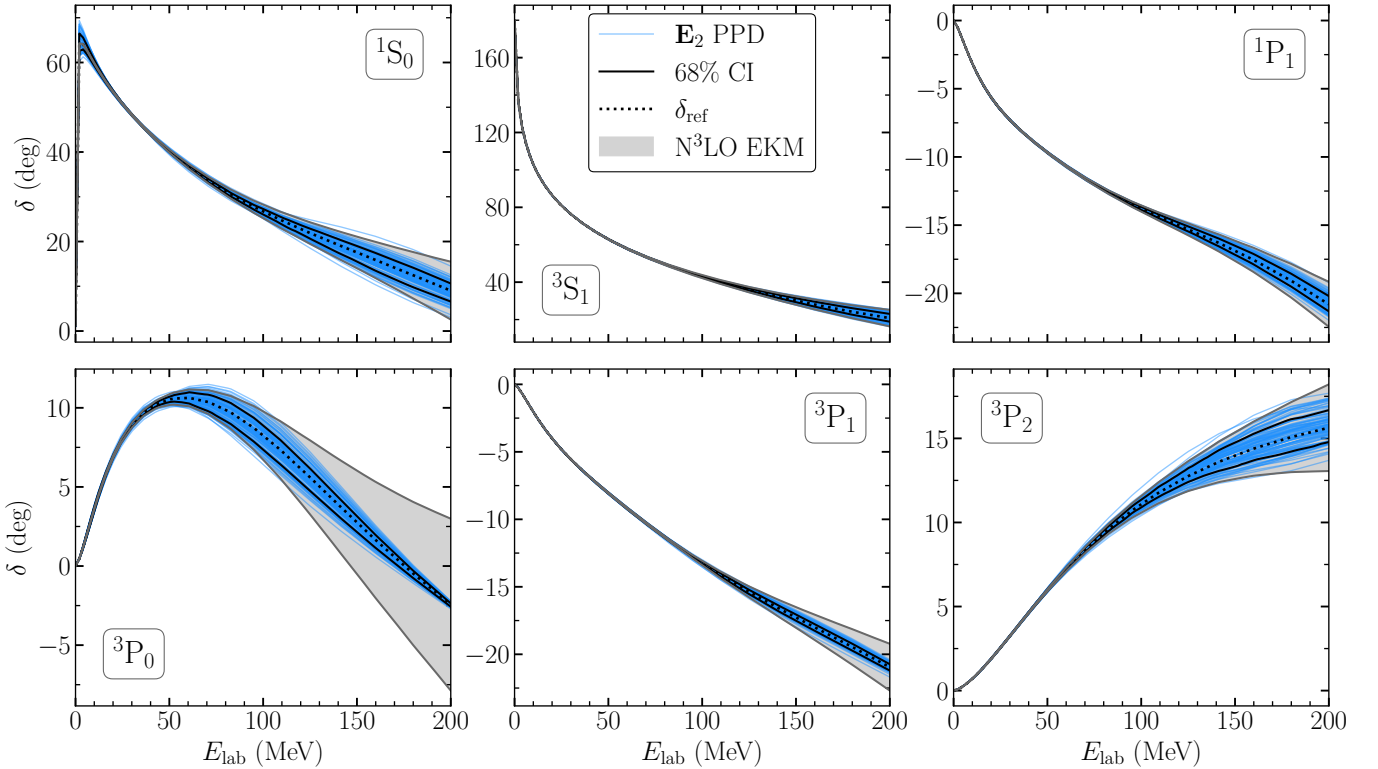


FIG. 6. Comparison of phase shifts PPDs in the 3S_1 partial wave using the E_1 likelihood (orange) and the E_2 likelihood (blue) at different energies. Shown are the 100 subsamples. The orange and blue dashed lines show the corresponding 68% confidence intervals. The solid black line represents the reference phase shifts obtained by using the EM 500 $\lambda = 1.8 \text{ fm}^{-1}$ interaction at N^3LO in SVD decomposition up to rank five. The black dashed lines represent the EKM uncertainty at N^3LO .

distributions. This is again due to correlations: stronger constraints on low-energy phase shifts result in stronger constraints at higher energies.

In Fig. 7, we show the same results in the 3P_0 partial wave. Note that we only vary two parameters in this partial wave because other operators are either not lin-

early independent from the two we include or produce no notable variations at energies below 200 MeV. Here we can see the same qualitative behavior as before, only more pronounced. Phase shift uncertainties are strongly overpredicted at low energies for the E_2 likelihood and underpredicted at high energies. Once again the operator

FIG. 7. Same as Fig. 6 for the 3P_0 partial wave.FIG. 8. Posterior phase shift distributions for the 100 subsamples in S- and P-waves based on the \mathbf{E}_2 likelihood. The dotted black line represents the reference phase shifts obtained by using the SVD-decomposed N^3LO EM 500 $\lambda = 1.8 \text{ fm}^{-1}$ interaction at rank five. The gray band represents the EKM uncertainty at N^3LO . The blue lines represent the individual samples, the black solid line corresponds to their 68% confidence intervals.

structure does not allow for phase shifts to vary independently at different energies. The \mathbf{E}_1 distributions describe the EKM uncertainty well at 1 MeV but underpredict it

at all higher energies.

We observe similar behavior in all partial waves. At low energies, \mathbf{E}_2 distributions overpredict the EFT un-

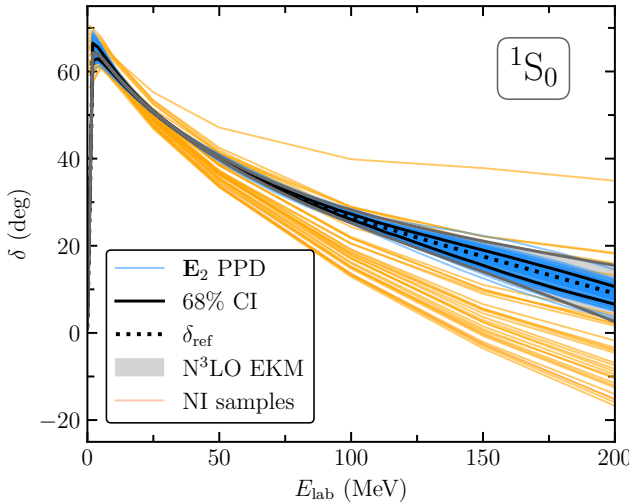


FIG. 9. Posterior phase shift distributions for the 100 subsamples in the 1S_0 partial wave based on the \mathbf{E}_2 likelihood. The dotted black line represents the reference phase shifts obtained by using the SVD-decomposed N^3LO EM $500 \lambda = 1.8 \text{ fm}^{-1}$ interaction at rank five. The gray band represents the EKM uncertainty at N^3LO . The blue lines represent the individual samples, the black solid line corresponds to their 68% confidence intervals. Shown in orange are the nonimplausible (NI) samples obtained from history matching in [10]. Note that the NI samples are constructed at N^2LO in Δ -full chiral EFT.

certainties while \mathbf{E}_1 distributions underpredict, and both underpredict EFT uncertainties at energies above 25 MeV. This can be seen in Fig. 8, where uncertainties are particularly underpredicted by the PPD at high energies in the 3P_0 partial wave. Based on this intuition we treat the \mathbf{E}_2 distributions as the more conservative uncertainty, while \mathbf{E}_1 distributions serve as the lower end of uncertainties. Note that the EKM uncertainty itself is already a conservative way of estimating uncertainties.

In Fig. 9, we show the subsampled PPD for phase shifts in the 1S_0 partial wave. The orange lines correspond to the 34 nonimplausible samples obtained through history matching from [10]. These samples estimate the parametric uncertainty of a Δ -full interaction at N^2LO . We compare to the posterior distribution of our \mathbf{E}_2 likelihood, noting that the distributions are constructed using EFT uncertainties at different orders (N^2LO for the nonimplausible samples vs. N^3LO in this work). This makes direct comparison challenging, but we gain insight into the effect of going to higher orders in chiral EFT and of using a more stringent likelihood sampling approach as compared to the conservative Pukelsheim's 3σ nonimplausibility criterion used in [10]. We conclude that our distribution is significantly more constrained than the nonimplausible samples across all energies considered.

Finally we turn our attention to the reproduction of input EFT uncertainties for our 3N observables. Figure 10 shows the posteriors for c_D and c_E marginalized over all NN parameters, as well as the PPDs for $E(^3\text{H})$ and

$fT_{1/2}$ for all 5×10^5 samples. These distributions shown here were obtained using the \mathbf{E}_2 likelihood, however the results for \mathbf{E}_1 are not noticeably different. The distributions for $E(^3\text{H})$ and $fT_{1/2}$ are essentially uncorrelated, further justifying the use of these two observables to constrain c_D and c_E . The black dashed lines represent one standard deviation of the uncertainty used to construct the 3N likelihood, as defined in Eq. (19). The blue band represents the 68% confidence interval of the PPD for the observables. The two intervals are in excellent agreement, indicating that our samples are distributed according to the 3N likelihood we constructed.

IV. APPLICATIONS TO MEDIUM-MASS NUCLEI

With two different posterior distributions for the parametric uncertainty of the 1.8/2.0 (EM) interaction at hand, we investigate their impact on nuclear structure calculations. We are in particular interested in quantifying the uncertainties in past predictions using the 1.8/2.0 (EM) Hamiltonian and comparing with other state-of-the-art approaches to quantifying uncertainties in nuclear structure calculations [10, 11, 21, 22, 51]. Other approaches assume zero correlation between the parametric uncertainty captured in the distribution of LECs and the EFT truncation uncertainty of nuclear structure observables. This results in an additive model of uncertainties

$$y = y_k + \delta_{\text{model}} + \delta_{\text{method}}, \quad (27)$$

where y_k contains parametric uncertainties, δ_{model} is the EFT truncation uncertainty, and δ_{method} the uncertainty due to other effects like many-body truncations. In our approach, the input LECs are fixed and only the singular values s_i are uncertain. Hence our “parametric uncertainty” is not driven by fitting errors but is constructed from truncation estimates in the NN and 3N sectors. In this setup truncation errors are already captured by the posterior distribution of singular values resulting from our Bayesian inference. Assuming perfect correlation between truncation uncertainties of these NN and 3N systems and medium-mass nuclei observables, we would be double counting uncertainties if we included an additional δ_{model} term for the target observable of interest, leading to too conservative uncertainties for nuclear structure predictions.

In this work, we focus on the parametric uncertainty, which we expect to capture a large part of the EFT truncation uncertainty in nuclear structure observables, and do not consider an additional explicit EFT truncation uncertainty δ_{model} . Note that we also do not consider a δ_{method} in this work. Under these assumptions our uncertainty model reduces to just the posterior predictive distribution from Eq. (26), i.e., the propagation of truncation-induced parametric uncertainties to target observables. Many bulk observables in nuclei are correlated,

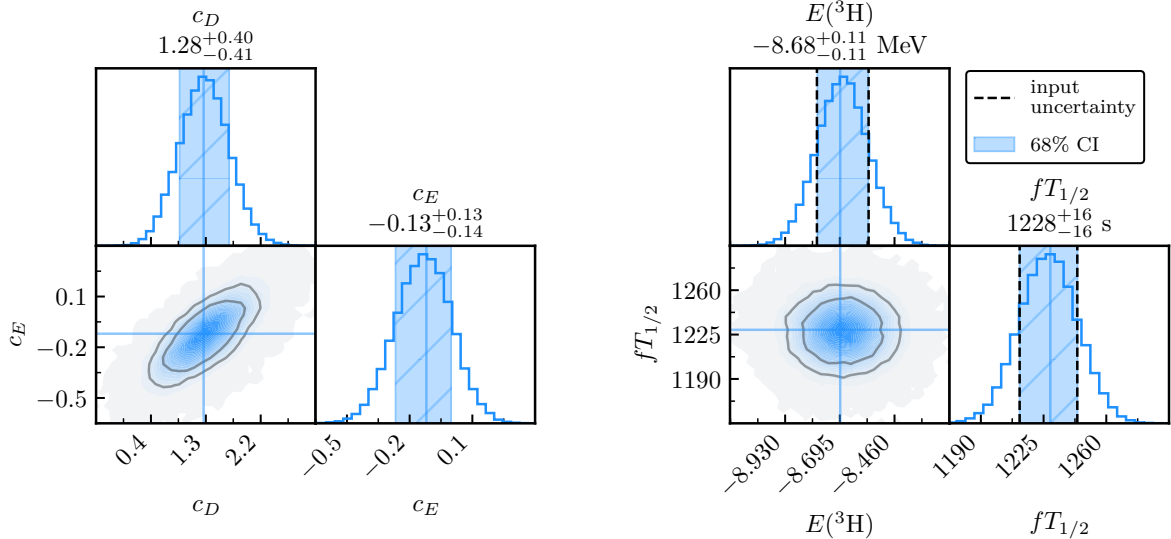


FIG. 10. Posterior distributions of c_D and c_E as well as posterior predictive distributions of $E(^3\text{H})$ and $fT_{1/2}$ for all 5×10^5 samples based on the \mathbf{E}_2 likelihood. The bottom left panel shows the joint probability distribution of c_D , c_E on the left and $fT_{1/2}$, $E(^3\text{H})$ on the right. Contours enclose 39% and 87% of the total probability, matching the fractions of a 1σ and 2σ contour for a 2D Gaussian. The top and right panels show the marginalized distributions of c_D and c_E on the left and $E(^3\text{H})$ and $fT_{1/2}$ on the right. The blue range shows the 68% CIs of the distributions. The black dashed lines denote the EFT truncation uncertainty used to construct the likelihood.

and so are the systematic theory uncertainties when computing them [10, 22, 51–55]. Developing a quantitative understanding how to handle correlations between the parametric and EFT truncation uncertainty is an important avenue for future work that is necessary for complete and accurate uncertainty quantification.

We compute the structure of oxygen and calcium isotopes using the in-medium similarity renormalization group (IMSRG) [56, 57], a well established quantum many-body method, truncated at the IMSRG(2) level. All calculations are preformed with the IMSRG++ code [58]. NN and 3N matrix elements are expanded in a spherical harmonic-oscillator (HO) basis with frequency $\hbar\omega = 16$ MeV and employing a truncation on the single-particle basis based on $e = 2n + l \leq e_{\text{max}} = 14$. For 3N matrix elements we employ an additional truncation on the three-body basis, including states $|123\rangle$ with $e_1 + e_2 + e_3 \leq E_{\text{max}}^{(3)} = 24$ [59]. We use an optimized basis consisting of Hartree-Fock and perturbatively improved natural orbital states following the construction of Ref. [53]. Finally, we apply a truncation of $e_{\text{max}} = 10$ to the natural orbitals.

We limit our investigations to oxygen and calcium isotopes in this work although the 100 samples can be applied to any nuclear structure calculation that is based on the 1.8/2.0 (EM) interaction. We investigate the impact of our different assumptions by calculating ^{24}O , ^{28}O , and ^{48}Ca observables using different variations of the 1.8/2.0 (EM) interaction. First, we use the unchanged 1.8/2.0 (EM) interaction. Then we use the same interaction but with SVD truncated S- and P-waves at $R_{\text{SVD}} = 5$. We also investigate the effect of the charge independence assumption

in the S- and P-waves on our observables by applying Eq. (18) to the S- and P-wave interactions. In a third variation we combine the two effects.

Table IV gives the ground-state energy, charge radius, and neutron skin thickness of ^{24}O , ^{28}O , and ^{48}Ca for the different modifications of the 1.8/2.0 (EM) interaction, together with the difference to the predictions using the unchanged 1.8/2.0 (EM) interaction. We notice that uncertainties caused by the SVD truncation are always below 1%. The charge-independence assumption causes deviations of up to 3% for energies. The deviations for charge radii and the neutron skins are still below 1% for all nuclei considered. Since we are more concerned with uncertainty estimates than reproducing the exact values for observables, this accuracy is sufficient. The uncertainty due to the SVD truncation can be easily improved in the future by simply adding the higher-order parts of the SVD that are discarded at the moment back to the interaction. For the charge-independence assumption, we avoid the explicit treatment of individual isospin channels and instead shift the median values of the distributions to the predictions using the unchanged 1.8/2.0 (EM) interaction.

In Fig. 11, we show the PPDs for the ground-state energy of ^{24}O . The distribution corresponding to the \mathbf{E}_1 likelihood is narrower than the \mathbf{E}_2 distribution, as expected. The resulting 68% confidence intervals around the shifted median are: $E(^{24}\text{O})_{\mathbf{E}_1} = -167.83^{+4.98}_{-5.09}$ MeV and $E(^{24}\text{O})_{\mathbf{E}_2} = -166.87^{+7.22}_{-5.85}$ MeV. We calculate the ratio of the widths of the two distributions for any interval $[x^{\text{low}}, x^{\text{high}}]$, as $r = (x_{\mathbf{E}_1}^{\text{high}} - x_{\mathbf{E}_1}^{\text{low}}) / (x_{\mathbf{E}_2}^{\text{high}} - x_{\mathbf{E}_2}^{\text{low}})$. Here, we get $r_{68\%} = 0.77$ and $r_{95\%} = 0.70$. The two distributions

TABLE IV. Computed observables for variations of the 1.8/2.0 (EM) interaction: “Unchanged” using the original 1.8/2.0 (EM) Hamiltonian; “SVD” after applying the rank-five SVD truncation in the S- and P-waves; “CII” using the charge-independent interaction approximation for the S- and P-waves; and “SVD & CII” with the two previous approximations combined. See main text for details. Δ indicates the difference to the result using the original 1.8/2.0 (EM) Hamiltonian.

Observable	Configuration	^{24}O		^{28}O		^{48}Ca	
		Value	Δ	Value	Δ	Value	Δ
E (MeV)	Unchanged	-164.01	—	-162.45	—	-415.77	—
	SVD	-164.12	-0.11	-162.59	-0.14	-416.12	-0.35
	CII	-168.59	-4.58	-167.39	-4.94	-426.39	-10.62
	SVD & CII	-168.70	-4.69	-167.53	-5.08	-426.75	-10.98
R_{skin} (fm)	Unchanged	0.4764	—	0.6713	—	0.1439	—
	SVD	0.4762	-0.0002	0.6709	-0.0004	0.1439	0.0000
	CII	0.4730	-0.0034	0.6667	-0.0046	0.1444	0.0005
	SVD & CII	0.4728	-0.0035	0.6663	-0.0050	0.1444	0.0005
R_{ch} (fm)	Unchanged	2.611	—	2.765	—	3.290	—
	SVD	2.611	0.000	2.764	0.000	3.290	0.000
	CII	2.599	-0.012	2.753	-0.012	3.276	-0.013
	SVD & CII	2.599	-0.012	2.752	-0.012	3.277	-0.013

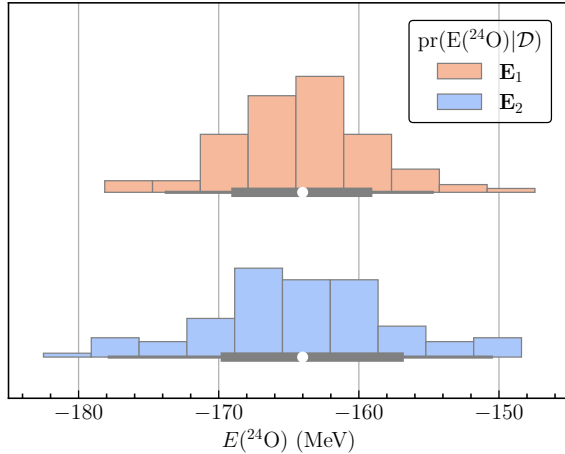


FIG. 11. PPDs for the ground-state energy of ^{24}O from the \mathbf{E}_1 and \mathbf{E}_2 likelihoods. The white dot shows the median while the thick and thin gray bars represent the 68% and 95% confidence intervals respectively. Note that the medians were shifted to reproduce the 1.8/2.0 (EM) interaction predictions.

only differ in the construction of their NN likelihoods. This shows us that the NN uncertainty significantly contributes to the uncertainty of the ground-state energy of ^{24}O , even though the uncertainties of the N^3LO NN interaction go as $(Q/\Lambda_b)^5$ and the N^2LO 3N uncertainties as $(Q/\Lambda_b)^4$. We compare our distributions to the results from [60]. Their uncertainties were obtained through a direct estimation of the EKM uncertainty of the binding energy of ^{24}O by assuming $Q = m_\pi$ and $\Lambda_b = 500$ MeV. Hence, these are purely chiral EFT truncation uncertainties. At N^3LO they receive $E(^{24}\text{O}) = -118.5^{+6.24}_{-6.24}$ MeV.

TABLE V. Uncertainty quantified predictions for ^{24}O , ^{28}O , and ^{48}Ca observables. The results are summarized by the medians and the 68% confidence intervals. In this table, results are not shifted to the median of the unchanged 1.8/2.0 (EM) Hamiltonian.

Nucleus	Observable	\mathbf{E}_1	\mathbf{E}_2
^{24}O	E (MeV)	$-167.83^{+4.98}_{-5.09}$	$-166.87^{+7.22}_{-5.85}$
^{28}O	E (MeV)	$-166.84^{+4.43}_{-4.71}$	$-165.76^{+5.89}_{-5.65}$
$^{28}\text{O} - ^{24}\text{O}$	ΔE (MeV)	$1.06^{+0.45}_{-0.41}$	$1.13^{+0.81}_{-0.97}$
^{48}Ca	E (MeV)	$-424.45^{+12.07}_{-13.61}$	$-421.61^{+19.43}_{-16.78}$
	R_{skin} (fm)	$0.1455^{+0.0018}_{-0.0017}$	$0.1449^{+0.0027}_{-0.0016}$
	R_{ch} (fm)	$3.288^{+0.032}_{-0.038}$	$3.288^{+0.058}_{-0.048}$

Note that the median value is significantly different than ours because of the different interaction used. The uncertainties are in a comparable range to ours, but it is important to remember that we consider a mixed order of N^2LO and N^3LO uncertainties, while [60] provides an $\text{NN} + \text{3N}$ N^3LO uncertainty estimate.

We also calculate the distribution of $E(^{28}\text{O})$, see Table V. By subtracting the ground-state energies of the two oxygen isotopes, we get the 4-neutron separation energy. We find that ^{28}O is a slightly unbound system, but we note that our calculations do not include continuum effects in the description of either ^{24}O or ^{28}O . Figure 12 shows the difference in ground-state energy between ^{28}O and ^{24}O . Here, the difference between the \mathbf{E}_1 and \mathbf{E}_2 distribution is even more significant with $\Delta E(^{28,24}\text{O})_{\mathbf{E}_1} = 1.56^{+0.45}_{-0.41}$ MeV and $\Delta E(^{28,24}\text{O})_{\mathbf{E}_2} = 1.56^{+0.81}_{-0.97}$ MeV, where we shifted the

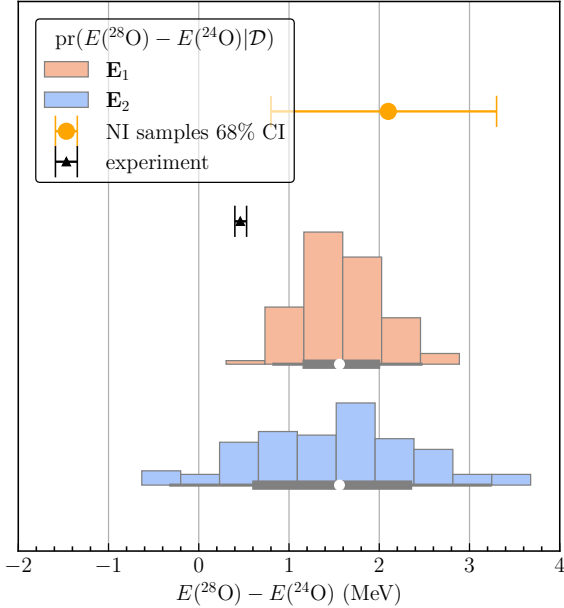


FIG. 12. PPDs for the difference between the ground-state energies of ^{28}O and ^{24}O from the \mathbf{E}_1 and \mathbf{E}_2 likelihoods. The white dot shows the median while the thick and thin gray bars represent the 68% and 95% confidence intervals respectively. Note that the medians were shifted to reproduce the 1.8/2.0 (EM) interaction predictions. The black triangle is experiment [11], and the orange dot and error bar represent the median and 68% confidence interval of the 121 nonimplausible samples from [11].

median values to the 1.8/2.0 (EM) prediction. The \mathbf{E}_2 distribution is twice as wide as the \mathbf{E}_1 distribution in terms of the 68% and 95% intervals, with $r_{68\%} = 0.49$, $r_{95\%} = 0.47$. The experimental value $\Delta E^{(28,24)\text{O}} = 0.46^{+0.05}_{-0.04}(\text{stat}) \pm 0.02(\text{syst})$ MeV falls slightly outside of the 68% confidence interval of our \mathbf{E}_2 distribution. For the \mathbf{E}_1 distribution, the experimental value is more than 2σ away $\Delta E^{(28,24)\text{O}}_{\mathbf{E}_1} = 1.56^{+0.45}_{-0.41}$ MeV. Again, continuum effects are not taken into account. Note that the deviation due to the charge-independence assumption for $\Delta E^{(28,24)\text{O}}$ is significantly larger than for the individual energies, because energy differences are smaller so that isospin symmetry breaking corrections are a larger effect for differential observables. We additionally compare to the distribution of 121 nonimplausible samples from [11]. These samples were obtained from history matching using Δ -full N²LO interactions and predict $\Delta E^{(28,24)\text{O}}_{\mathbf{E}_2} = 2.1^{+1.2}_{-1.3}$ MeV.

For ^{48}Ca , we consider the charge radius and the neutron skin thickness in addition to the ground-state energy. The charge radius is calculated as

$$R_{\text{ch}} = \langle R_{\text{p}}^2 \rangle + \langle r_{\text{so}}^2 \rangle + r_{\text{p}}^2 + \frac{N}{Z} r_{\text{n}}^2 + \frac{3}{4M^2}, \quad (28)$$

with the squared point-proton radius R_{p}^2 , the spin-orbit correction r_{so}^2 [53, 61], the Darwin-Foldy correction $3/(4M^2) = 0.033 \text{ fm}^2$ [62], and the squared proton

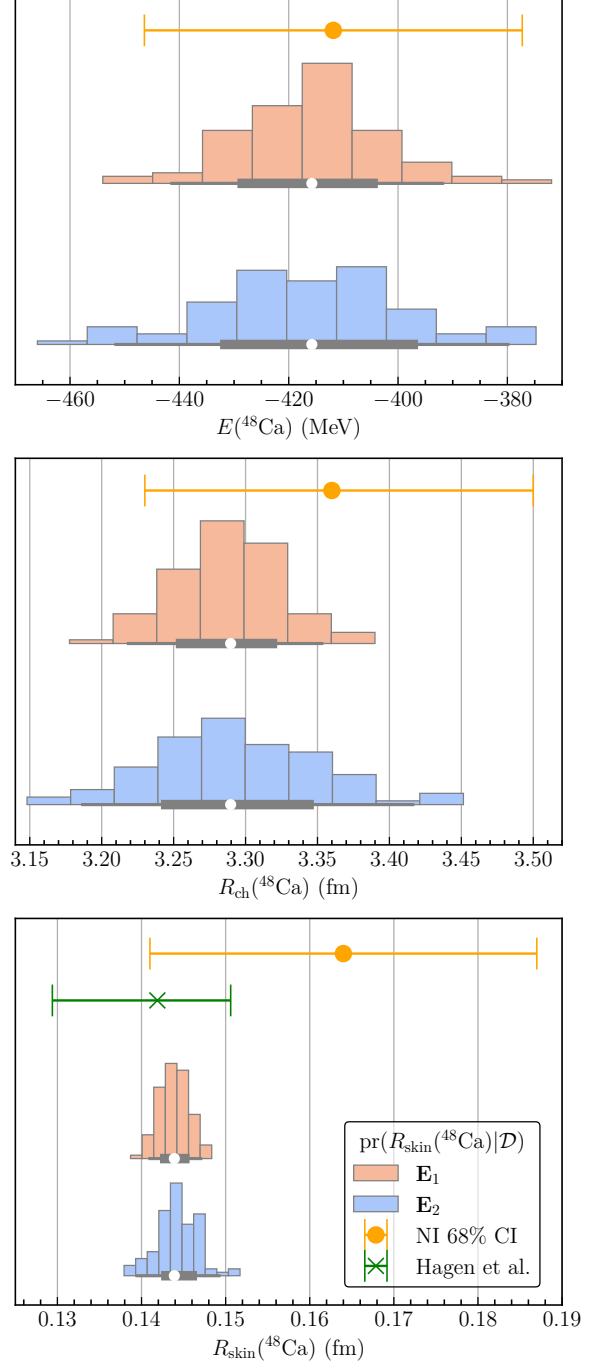


FIG. 13. PPDs for the ground-state energy (top panel), charge radius (middle panel), and neutron skin (bottom panel) of ^{48}Ca using the \mathbf{E}_1 and \mathbf{E}_2 results. The white dot shows the median while the thick and thin gray bars represent the 68% and 95% confidence intervals respectively. Note that the medians were shifted to reproduce the 1.8/2.0 (EM) interaction results. The orange dot and error bar represent the median and 68% confidence interval of the 34 nonimplausible results from [10]. The green band shows the range of *ab initio* predictions using six chiral interactions from [51].

charge radius $r_{\text{p}}^2 = 0.707 \text{ fm}^2$ and neutron charge radius

$r_n^2 = -0.115 \text{ fm}^2$ [63]. We compute the neutron skin

$$R_{\text{skin}} = \langle R_n^2 \rangle^{1/2} - \langle R_p^2 \rangle^{1/2}, \quad (29)$$

with the root-mean-square point-neutron and point-proton radii. The values $\langle r_{\text{so}}^2 \rangle$, $\langle R_p^2 \rangle$, and $\langle R_n^2 \rangle$ are obtained from the IMSRG by transforming the corresponding operators with the same unitary transformation as the Hamiltonian using the Magnus expansion [64].

In Fig. 13, we provide the posterior distributions for the ground-state energy, the charge radius, and the neutron skin thickness of ^{48}Ca . Comparing the distributions from the \mathbf{E}_1 and \mathbf{E}_2 likelihoods, the \mathbf{E}_1 distributions have roughly 70% of the width of the \mathbf{E}_2 distributions for all three observables. For comparison, we also show the 68% confidence intervals of the 34 nonimplausible samples from Hu *et al.* [10], and for the neutron skin we also show the range of *ab initio* predictions from six chiral interactions from Hagen *et al.* [51]. The orange lines show the 68% confidence intervals of the nonimplausible samples, which are significantly wider than our distributions. For all three observables our distributions overlap with the nonimplausible distributions, and for the neutron skin with those from the different chiral interactions. The resulting confidence intervals with median values not shifted to the unchanged 1.8/2.0 (EM) results for the different oxygen and calcium observables are given in Table V.

V. SUMMARY AND CONCLUSION

We have developed a framework to quantify EFT truncation uncertainties for low-resolution interactions. We obtained a linear operator structure for SRG-evolved NN interactions through singular value decompositions. We used the sensitivity of low-energy phase shifts to identify relevant low-energy operators. With a parametric description of the interaction at hand, we performed Bayesian inference for the underlying singular values. We constructed the likelihood for the inference from predictions for NN scattering phase shifts in S- and P-waves and for the triton energy and comparative half life. For NN phase shifts, we considered two likelihoods, both using phase shifts at energies up to 200 MeV. Phase shifts at different energies are treated as uncorrelated quantities, a simplification that can be improved in future work through the construction of correlated EFT truncation models using Gaussian processes. One likelihood, \mathbf{E}_2 , is more conservative than the other \mathbf{E}_1 , including less information about low-energy phase shifts in the construction.

Based on the combined NN and 3N likelihoods, we performed Bayesian inference for the singular values in our NN potentials and for c_D and c_E in our 3N potentials. We performed model checking for the inferred parameter distributions. We found that the input 3N likelihood is accurately reproduced by our posterior Hamiltonian distributions. On the other hand, we found that for the NN phase shifts they did not exactly reproduce the

likelihood as expected for unconstrained uniform priors. We concluded that the limited amount of independent operators in each partial wave and untreated correlations in phase shifts are responsible for these shortcomings.

Finally, we propagated the Hamiltonian uncertainties to medium-mass nuclei through IMSRG calculations using Hamiltonians sampled from our posterior distribution. We calculated PPDs for the ground-state energies of ^{24}O , ^{28}O , and the difference $\Delta E(^{28,24}\text{O})$. We found that our more conservative distribution based on the \mathbf{E}_2 likelihood is compatible with experiment for $\Delta E(^{28,24}\text{O})$. We also calculated PPDs for the energy, charge radius, and neutron skin thickness of ^{48}Ca . We compared our distributions to existing estimates of uncertainties for these observables. Our uncertainties were significantly smaller than the more conservative history matching results.

Our work focuses on capturing EFT truncation uncertainties in the distribution of underlying parameters in our Hamiltonian, commonly called parametric uncertainty. Through the inclusion of EFT truncation uncertainties in the Bayesian inference, the parametric uncertainty is closely related to the actual EFT truncation uncertainty. For full uncertainty quantification in nuclear structure calculations, the parametric uncertainty must be augmented with additional EFT truncation and many-body method uncertainties. A key challenge here is that these three uncertainties (parametric, EFT truncation, and many-body method) are all correlated, but this correlation is challenging to study quantitatively and needs further work. A systematic study of correlations between truncation uncertainties of observables across nuclei remains an important subject for future research.

ACKNOWLEDGMENTS

We thank Christian Forssén, Dick Furnstahl, Hannah Göttling, Takayuki Miyagi, Daniel Phillips, and Isak Svensson for helpful discussions. This work was supported in part by the European Research Council (ERC) under the European Union’s Horizon 2020 research and innovation programme (Grant Agreement No. 101020842), by the Deutsche Forschungsgemeinschaft (DFG, German Research Foundation) – Project-ID 279384907 – SFB 1245, by the Laboratory Directed Research and Development Program of Oak Ridge National Laboratory, managed by UT-Battelle, LLC, for the U.S. Department of Energy, by the U.S. Department of Energy, Office of Science, Office of Nuclear Physics under Award No. DE-SC0024586, and by the U.S. Department of Energy, Office of Science, Office of Advanced Scientific Computing Research and Office of Nuclear Physics, Scientific Discovery through Advanced Computing (SciDAC) program (SciDAC-5 NUCLEI). This research used resources of the Oak Ridge Leadership Computing Facility located at Oak Ridge National Laboratory, which is supported by the Office of Science of the Department of Energy under contract No. DE-AC05-00OR22725. The authors gratefully ac-

knowledge the Gauss Centre for Supercomputing e.V. (www.gauss-centre.eu) for funding this project by providing computing time through the John von Neumann Institute for Computing (NIC) on the GCS Supercomputer JUWELS at Jülich Supercomputing Centre (JSC)

and the computing time provided to them on the high-performance computer Lichtenberg II at TU Darmstadt, funded by the German Federal Ministry of Education and Research (BMBF) and the State of Hesse.

[1] E. Epelbaum, H.-W. Hammer, and U.-G. Meißner, Modern theory of nuclear forces, *Rev. Mod. Phys.* **81**, 1773 (2009), [arXiv:0811.1338](https://arxiv.org/abs/0811.1338).

[2] R. Machleidt and D. R. Entem, Chiral effective field theory and nuclear forces, *Phys. Rep.* **503**, 1 (2011), [arXiv:1105.2919](https://arxiv.org/abs/1105.2919).

[3] H.-W. Hammer, S. König, and U. van Kolck, Nuclear effective field theory: Status and perspectives, *Rev. Mod. Phys.* **92**, 025004 (2020), [arXiv:1906.12122](https://arxiv.org/abs/1906.12122).

[4] R. J. Furnstahl, D. R. Phillips, and S. Wesolowski, A recipe for EFT uncertainty quantification in nuclear physics, *J. Phys. G* **42**, 034028 (2015), [arXiv:1407.0657](https://arxiv.org/abs/1407.0657).

[5] R. J. Furnstahl, N. Klco, D. R. Phillips, and S. Wesolowski, Quantifying truncation errors in effective field theory, *Phys. Rev. C* **92**, 024005 (2015), [arXiv:1506.01343](https://arxiv.org/abs/1506.01343).

[6] E. Epelbaum, H. Krebs, and U.-G. Meißner, Improved chiral nucleon-nucleon potential up to next-to-next-to-next-to-leading order, *Eur. Phys. J. A* **51**, 53 (2015), [arXiv:1412.0142](https://arxiv.org/abs/1412.0142).

[7] S. Binder, A. Calci, E. Epelbaum, R. J. Furnstahl, J. Gollak, K. Hebeler, H. Kamada, H. Krebs, J. Langhammer, S. Liebig, *et al.* (LENPIC Collaboration), Few-nucleon systems with state-of-the-art chiral nucleon-nucleon forces, *Phys. Rev. C* **93**, 044002 (2016), [arXiv:1505.07218](https://arxiv.org/abs/1505.07218).

[8] B. D. Carlsson, A. Ekström, C. Forssén, D. F. Strömberg, G. R. Jansen, O. Lilja, M. Lindby, B. A. Mattsson, and K. A. Wendt, Uncertainty analysis and order-by-order optimization of chiral nuclear interactions, *Phys. Rev. X* **6**, 011019 (2016), [arXiv:1506.02466](https://arxiv.org/abs/1506.02466).

[9] J. A. Melendez, S. Wesolowski, and R. J. Furnstahl, Bayesian truncation errors in chiral effective field theory: nucleon-nucleon observables, *Phys. Rev. C* **96**, 024003 (2017), [arXiv:1704.03308](https://arxiv.org/abs/1704.03308).

[10] B. S. Hu, W. G. Jiang, T. Miyagi, Z. H. Sun, A. Ekström, C. Forssén, G. Hagen, J. D. Holt, T. Papenbrock, S. R. Stroberg, and I. Vernon, Ab initio predictions link the neutron skin of ^{208}Pb to nuclear forces, *Nat. Phys.* **18**, 1196 (2022), [arXiv:2112.01125](https://arxiv.org/abs/2112.01125).

[11] Y. Kondo, N. L. Achouri, H. Al Falou, L. Atar, T. Aumann, H. Baba, K. Boretzky, C. Caesar, D. Calvet, H. Chae, *et al.*, First observation of ^{28}O , *Nature* **620**, 965 (2023).

[12] I. Svensson, A. Tichai, K. Hebeler, and A. Schwenk, A Bayesian approach for many-body uncertainties in nuclear structure: Many-body perturbation theory for finite nuclei, [arXiv:2507.09079](https://arxiv.org/abs/2507.09079).

[13] S. K. Bogner, R. J. Furnstahl, and A. Schwenk, From low-momentum interactions to nuclear structure, *Prog. Part. Nucl. Phys.* **65**, 94 (2010), [arXiv:0912.3688](https://arxiv.org/abs/0912.3688).

[14] K. Hebeler, S. K. Bogner, R. J. Furnstahl, A. Nogga, and A. Schwenk, Improved nuclear matter calculations from chiral low-momentum interactions, *Phys. Rev. C* **83**, 031301(R) (2011), [arXiv:1012.3381](https://arxiv.org/abs/1012.3381).

[15] G. Hagen, G. R. Jansen, and T. Papenbrock, Structure of ^{78}Ni from first-principles computations, *Phys. Rev. Lett.* **117**, 172501 (2016), [arXiv:1605.01477](https://arxiv.org/abs/1605.01477).

[16] J. Simonis, S. R. Stroberg, K. Hebeler, J. D. Holt, and A. Schwenk, Saturation with chiral interactions and consequences for finite nuclei, *Phys. Rev. C* **96**, 014303 (2017), [arXiv:1704.02915](https://arxiv.org/abs/1704.02915).

[17] T. D. Morris, J. Simonis, S. R. Stroberg, C. Stumpf, G. Hagen, J. D. Holt, G. R. Jansen, T. Papenbrock, R. Roth, and A. Schwenk, Structure of the lightest tin isotopes, *Phys. Rev. Lett.* **120**, 152503 (2018), [arXiv:1709.02786](https://arxiv.org/abs/1709.02786).

[18] S. R. Stroberg, J. D. Holt, A. Schwenk, and J. Simonis, *Ab initio* limits of atomic nuclei, *Phys. Rev. Lett.* **126**, 022501 (2021), [arXiv:1905.10475](https://arxiv.org/abs/1905.10475).

[19] P. Arthuis, K. Hebeler, and A. Schwenk, Neutron-rich nuclei and neutron skins from chiral low-resolution interactions, [arXiv:2401.06675](https://arxiv.org/abs/2401.06675).

[20] F. Bonaiti, G. Hagen, and T. Papenbrock, Structure of the doubly magic nuclei ^{208}Pb and ^{266}Pb from ab initio computations, [arXiv:2508.14217](https://arxiv.org/abs/2508.14217).

[21] T. Hüther, K. Vobig, K. Hebeler, R. Machleidt, and R. Roth, Family of Chiral Two- plus Three-Nucleon Interactions for Accurate Nuclear Structure Studies, *Phys. Lett. B* **808**, 135651 (2020), [arXiv:1911.04955](https://arxiv.org/abs/1911.04955).

[22] P. Maris, R. Roth, E. Epelbaum, R. J. Furnstahl, J. Gollak, K. Hebeler, T. Hüther, H. Kamada, H. Krebs, H. Le, *et al.* (LENPIC Collaboration), Nuclear properties with semilocal momentum-space regularized chiral interactions beyond N^2LO , *Phys. Rev. C* **106**, 064002 (2022), [arXiv:2206.13303](https://arxiv.org/abs/2206.13303).

[23] A. Tichai, P. Arthuis, K. Hebeler, M. Heinz, J. Hoppe, and A. Schwenk, Low-rank matrix decompositions for *ab initio* nuclear structure, *Phys. Lett. B* **821**, 136623 (2021), [arXiv:2105.03935](https://arxiv.org/abs/2105.03935).

[24] B. Zhu, R. Wirth, and H. Hergert, Singular value decomposition and similarity renormalization group evolution of nuclear interactions, *Phys. Rev. C* **104**, 044002 (2021), [arXiv:2106.01302](https://arxiv.org/abs/2106.01302).

[25] A. Tichai, P. Arthuis, K. Hebeler, M. Heinz, J. Hoppe, A. Schwenk, and L. Zurek, Least-square approach for singular value decompositions of scattering problems, *Phys. Rev. C* **106**, 024320 (2022), [arXiv:2205.10087](https://arxiv.org/abs/2205.10087).

[26] A. Tichai, P. Arthuis, K. Hebeler, M. Heinz, J. Hoppe, T. Miyagi, A. Schwenk, and L. Zurek, Randomized low-rank decompositions of nuclear three-body interactions, *Phys. Rev. Res.* **6**, 043331 (2024), [arXiv:2307.15572](https://arxiv.org/abs/2307.15572).

[27] D. Frame, R. He, I. Ipsen, D. Lee, D. Lee, and E. Rrapaj, Eigenvector continuation with subspace learning, *Phys. Rev. Lett.* **121**, 032501 (2018), [arXiv:1711.07090](https://arxiv.org/abs/1711.07090).

[28] S. König, A. Ekström, K. Hebeler, D. Lee, and A. Schwenk, Eigenvector continuation as an efficient and accurate emulator for uncertainty quantification, *Phys. Lett. B* **810**, 135814 (2020), [arXiv:1909.08446](https://arxiv.org/abs/1909.08446).

[29] T. Duguet, A. Ekström, R. J. Furnstahl, S. König, and D. Lee, Colloquium: Eigenvector continuation and

projection-based emulators, *Rev. Mod. Phys.* **96**, 031002 (2024), arXiv:2310.19419.

[30] S. Wesolowski, N. Klco, R. J. Furnstahl, D. R. Phillips, and A. Thapaliya, Bayesian parameter estimation for effective field theories, *J. Phys. G* **43**, 074001 (2016), arXiv:1511.03618.

[31] S. Wesolowski, R. J. Furnstahl, J. A. Melendez, and D. R. Phillips, Exploring Bayesian parameter estimation for chiral effective field theory using nucleon-nucleon phase shifts, *J. Phys. G* **46**, 045102 (2019), arXiv:1808.08211.

[32] A. Ekström and G. Hagen, Global sensitivity analysis of bulk properties of an atomic nucleus, *Phys. Rev. Lett.* **123**, 252501 (2019), arXiv:1910.02922.

[33] W. G. Jiang and C. Forssén, Bayesian probability updates using sampling/importance resampling: Applications in nuclear theory, *Front. Phys.* **10**, 1058809 (2022), arXiv:2210.02507.

[34] I. Svensson, A. Ekström, and C. Forssén, Bayesian parameter estimation in chiral effective field theory using the Hamiltonian Monte Carlo method, *Phys. Rev. C* **105**, 014004 (2022), arXiv:2110.04011.

[35] I. Svensson, A. Ekström, and C. Forssén, Bayesian estimation of the low-energy constants up to fourth order in the nucleon-nucleon sector of chiral effective field theory, *Phys. Rev. C* **107**, 014001 (2023), arXiv:2206.08250.

[36] I. Svensson, A. Ekström, and C. Forssén, Inference of the low-energy constants in Δ -full chiral effective field theory including a correlated truncation error, *Phys. Rev. C* **109**, 064003 (2024), arXiv:2304.02004.

[37] D. R. Entem and R. Machleidt, Accurate charge-dependent nucleon-nucleon potential at fourth order of chiral perturbation theory, *Phys. Rev. C* **68**, 041001(R) (2003), arXiv:nucl-th/0304018.

[38] S. K. Bogner, R. J. Furnstahl, and R. J. Perry, Similarity renormalization group for nucleon-nucleon interactions, *Phys. Rev. C* **75**, 061001(R) (2007), arXiv:nucl-th/0611045.

[39] S. K. Bogner, R. J. Furnstahl, P. Maris, R. J. Perry, A. Schwenk, and J. P. Vary, Convergence in the no-core shell model with low-momentum two-nucleon interactions, *Nucl. Phys. A* **801**, 21 (2008), arXiv:0708.3754.

[40] C. Drischler, J. A. Melendez, R. J. Furnstahl, and D. R. Phillips, Quantifying uncertainties and correlations in the nuclear-matter equation of state, *Phys. Rev. C* **102**, 054315 (2020), arXiv:2004.07805.

[41] S. Wesolowski, I. Svensson, A. Ekström, C. Forssén, R. J. Furnstahl, J. A. Melendez, and D. R. Phillips, Rigorous constraints on three-nucleon forces in chiral effective field theory from fast and accurate calculations of few-body observables, *Phys. Rev. C* **104**, 064001 (2021), arXiv:2104.04441.

[42] A. Ekström and L. Platter, Quantifying the breakdown scale of pionless effective field theory, *Phys. Lett. B* **860**, 139207 (2025), arXiv:2409.08197.

[43] D. R. Entem, R. Machleidt, and Y. Nosyk, High-quality two-nucleon potentials up to fifth order of the chiral expansion, *Phys. Rev. C* **96**, 024004 (2017), arXiv:1703.05454.

[44] J. A. Melendez, R. J. Furnstahl, D. R. Phillips, M. T. Pratola, and S. Wesolowski, Quantifying correlated truncation errors in effective field theory, *Phys. Rev. C* **100**, 044001 (2019), arXiv:1904.10581.

[45] D. Gazit, S. Quaglioni, and P. Navratil, Three-Nucleon Low-Energy Constants from the Consistency of Interactions and Currents in Chiral Effective Field Theory, *Phys. Rev. Lett.* **103**, 102502 (2009), [Erratum: *Phys. Rev. Lett.* **122**, 029901 (2019)], arXiv:0812.4444.

[46] T. Miyagi, private communication (2024).

[47] R. Schiavilla, V. Stoks, W. Glöckle, H. Kamada, A. Nogga, J. Carlson, R. Machleidt, V. Pandharipande, R. B. Wiringa, A. Kievsky, *et al.*, Weak capture of protons by protons, *Phys. Rev. C* **58**, 1263 (1998).

[48] S. Fiarman and S. S. Hanna, Energy levels of light nuclei $A = 3$, *Nucl. Phys. A* **251**, 1 (1975).

[49] Y. A. Akulov and B. A. Mamyrin, Half-life and $fT_{1/2}$ value for the bare triton, *Phys. Lett. B* **610**, 45 (2005).

[50] D. Foreman-Mackey, D. W. Hogg, D. Lang, and J. Goodman, emcee: the MCMC hammer, *Publ. Astron. Soc. Pac.* **125**, 306 (2013).

[51] G. Hagen, A. Ekström, C. Forssén, G. R. Jansen, W. Nazarewicz, T. Papenbrock, K. A. Wendt, S. Bacca, N. Barnea, B. Carlsson, C. Drischler, K. Hebeler, M. Hjorth-Jensen, M. Miorelli, G. Orlandini, A. Schwenk, and J. Simonis, Neutron and weak-charge distributions of the ^{48}Ca nucleus, *Nat. Phys.* **12**, 186 (2016), arXiv:1509.07169.

[52] L. Neufcourt, Y. Cao, W. Nazarewicz, and F. Viens, Bayesian approach to model-based extrapolation of nuclear observables, *Phys. Rev. C* **98**, 034318 (2018), arXiv:1806.00552.

[53] M. Heinz, T. Miyagi, S. R. Stroberg, A. Tichai, K. Hebeler, and A. Schwenk, Improved structure of calcium isotopes from ab initio calculations, *Phys. Rev. C* **111**, 034311 (2025), arXiv:2411.16014.

[54] M. Heinz, M. Hoferichter, T. Miyagi, F. Nöel, and A. Schwenk, Ab initio calculations of overlap integrals for $\mu \rightarrow e$ conversion in nuclei, arXiv:2412.04545.

[55] T. Miyagi, M. Heinz, and A. Schwenk, Ab initio computations of the fourth-order charge density moments of ^{48}Ca and ^{208}Pb , arXiv:2508.10767.

[56] K. Tsukiyama, S. K. Bogner, and A. Schwenk, In-medium similarity renormalization group for nuclei, *Phys. Rev. Lett.* **106**, 222502 (2011), arXiv:1006.3639.

[57] H. Hergert, S. K. Bogner, T. D. Morris, A. Schwenk, and K. Tsukiyama, The in-medium similarity renormalization group: A novel *ab initio* method for nuclei, *Phys. Rep.* **621**, 165 (2016), arXiv:1512.06956.

[58] S. R. Stroberg *et al.*, <https://github.com/ragnarstroberg/imsrg> (2024).

[59] T. Miyagi, S. R. Stroberg, P. Navrátil, K. Hebeler, and J. D. Holt, Converged *ab initio* calculations of heavy nuclei, *Phys. Rev. C* **105**, 014302 (2022), arXiv:2104.04688.

[60] J. Hoppe, C. Drischler, K. Hebeler, A. Schwenk, and J. Simonis, Probing chiral interactions up to next-to-next-to-next-to-leading order in medium-mass nuclei, *Phys. Rev. C* **100**, 024318 (2019), arXiv:1904.12611.

[61] A. Ong, J. C. Berengut, and V. V. Flambaum, Effect of spin-orbit nuclear charge density corrections due to the anomalous magnetic moment on halonuclei, *Phys. Rev. C* **82**, 014320 (2010), arXiv:1006.5508.

[62] J. L. Friar, J. Martorell, and D. W. L. Sprung, Nuclear sizes and the isotope shift, *Phys. Rev. A* **56**, 4579 (1997), arXiv:nucl-th/9707016.

[63] R. L. Workman *et al.* (Particle Data Group), Review of particle physics, *Prog. Theor. Exp. Phys.* **2022**, 083C01 (2022).

[64] T. D. Morris, N. M. Parzuchowski, and S. K. Bogner, Magnus expansion and in-medium similarity renormalization group, *Phys. Rev. C* **92**, 034331 (2015), arXiv:1507.06725.